

THESIS FOR THE DEGREE OF DOCTOR OF PHILOSOPHY

Characterization of Fe-W alloys electrodeposited from environmentally friendly electrolyte

Antonio Mulone

Department of Industrial and Materials Science  
CHALMERS UNIVERSITY OF TECHNOLOGY

Gothenburg, Sweden 2020

Characterization of Fe-W alloys electrodeposited from environmentally friendly electrolyte  
ANTONIO MULONE  
ISBN 978-91-7905-256-0

© ANTONIO MULONE, 2020.

Doktorsavhandlingar vid Chalmers tekniska högskola  
Ny serie nr 4723  
ISSN 0346-718X

Department of Industrial and Materials Science  
Chalmers University of Technology  
SE-412 96 Gothenburg  
Sweden  
Telephone + 46 (0)31-772 1000

Chalmers Reproservice  
Gothenburg, Sweden 2020

# Characterization of Fe-W alloys electrodeposited from environmentally friendly electrolyte

ANTONIO MULONE

Department of Industrial and Materials Science  
Chalmers University of Technology

## Abstract

This work focuses on Fe-W and Fe-W/Al<sub>2</sub>O<sub>3</sub> coatings electrodeposited from an environmentally friendly electrolyte: minimally invasive, thermodynamically stable, and without toxic compounds. Such coatings aim to be applied for protective applications and as a sustainable alternative to hard chromium coatings. Therefore, the goal of this thesis is to evaluate the interdependencies between the material characteristics (e.g. composition and structure) and the properties of interest: the mechanical properties as well as wear and corrosion resistance. The structure of the coatings was investigated with various analytical techniques (e.g. XRD, SEM, EBSD, and TEM among others), both in the as-deposited state and after heat treatments. Heat treatments led to microstructural transformations in the Fe-W coatings. Nanohardness and wear measurements were performed to study the influence of such microstructural changes on the mechanical properties and wear resistance of the Fe-W coatings.

The results included in this thesis show that increasing the amount of co-deposited W in the coatings results in a transition from a nanocrystalline to a homogeneous amorphous structure, and to an increase in the thermal stability. In-situ TEM analyses on W-rich coatings (i.e. Fe-24at.%W) revealed the formation of crystallites at 400 °C within the amorphous matrix. Moreover, a large fraction of the amorphous structure is still preserved upon annealing at 600 °C, where  $\alpha$ -Fe nanocrystals are found. The microstructural transformations result in an enhancement of mechanical properties of Fe-W coatings. The Fe-24at.%W coating is characterized with the highest hardness both in the as-deposited and annealed state, where a maximum value of 16.5 GPa is observed after annealing at 600 °C. However, Fe-W coatings are characterized with rather low wear resistance due to severe tribo-oxidation resulting in high coefficient of friction (COF) and wear rates. A considerable improvement in the wear resistance is obtained with the co-deposition of ~12vol.% of Al<sub>2</sub>O<sub>3</sub> particles leading to a reduction in the COF and wear rate. The influence of the co-deposited alumina particles on the corrosion resistance is rather limited, i.e. similar values of the corrosion current are measured for the both the Fe-W/Al<sub>2</sub>O<sub>3</sub> composites and Fe-W coatings. Annealing at 600 °C of Fe-W/12%Al<sub>2</sub>O<sub>3</sub> composite leads to a combination of high hardness and high wear resistance which result superior to the hardness and wear resistance of hard chromium coatings.

**Keywords:** Electrodeposition, Fe-W alloys, Sustainability, Heat treatments, EBSD, TEM, Hardness, Wear.



## Preface

This thesis is based on work carried out at the Department of Industrial and Materials Science at Chalmers University of Technology in the time between September 2015 and March 2020. Part of the work was performed in connection with the project SELECTA (Smart ELECTrodeposited Alloys for environmentally sustainable applications: from advanced protective coatings to micro/nano-robotic platforms, H2020-MSCA-ITN-2014 No 642642). The work was supervised by Prof. Uta Klement.

The thesis consists of an introductory part followed by the appended papers listed below:

- Paper I:** Electrodeposition: three steps toward sustainability  
A. Mulone, J. Hildenbrand, U. Klement  
*Accepted for publication in Transaction of the IMF after revision.*
- Paper II:** In-depth characterization of as-deposited and annealed Fe-W coatings electrodeposited from glycolate-citrate plating bath  
A. Mulone, A. Nicolenco, V. Hoffmann, U. Klement, N. Tsyntaru, H. Cesiulis  
*Electrochimica Acta, Volume 261, Pages 167-177, 2018.*
- Paper III:** Enhanced mechanical properties and microstructural modifications in electrodeposited Fe-W alloys through controlled heat treatments  
A. Mulone, A. Nicolenco, J. Fornell, E. Pellicer, N. Tsyntaru, H. Cesiulis, J. Sort, U. Klement  
*Surface and Coatings Technology, Volume 350, Pages 20-30, 2018.*
- Paper IV:** In-situ TEM annealing of amorphous Fe-24at.%W coatings and the effect of crystallization on hardness  
A. Mulone, I. Ennen, A. Hütten, U. Klement  
*In manuscript.*
- Paper V:** Improvement in the wear resistance under dry friction of electrodeposited Fe-W coatings through heat treatments  
A. Mulone, A. Nicolenco, N. Imaz, V. Martina-Nogues, N. Tsyntaru, H. Cesiulis, U. Klement  
*Coatings, Volume 9, Page 66, 2019.*
- Paper VI:** Nanocrystalline electrodeposited Fe-W/Al<sub>2</sub>O<sub>3</sub> composites: effect of alumina sub-microparticles on the mechanical, tribological, and corrosion properties  
A. Nicolenco, A. Mulone, N. Imaz, N. Tsyntaru, J. Sort, E. Pellicer, U. Klement, H. Cesiulis, E. Garcia-Lecina  
*Frontiers in Chemistry, Volume 7, Page 241, 2019.*
- Paper VII:** Electrodeposited Fe-W/Al<sub>2</sub>O<sub>3</sub> composites: effect of heat treatments on the mechanical and tribological properties  
A. Mulone, A. Nicolenco, N. Imaz, J. Fornell, J. Sort, U. Klement  
*Wear, Pages 448-449, 2020.*

## **Contribution to the appended papers**

- Paper I:** The planning was conducted in collaboration with the co-authors. The author wrote the first draft of the paper.
- Paper II:** The author conducted most of the experimental work, i.e. SEM, XRD and annealing treatments. TEM analyses were performed together with Dr. Yiming Yao. The GDOES measurements were performed at IFW Dresden. The results were analysed and discussed with all co-authors. The author wrote the first draft of the paper.
- Paper III:** The author conducted the experimental work. The nanoindentation measurements were performed at the Department de Física of the Universitat Autònoma de Barcelona. The author wrote the first draft of the paper.
- Paper IV:** The in-situ TEM measurements were performed at the University of Bielefeld together with Dr. Inga Ennen. The author wrote the first draft of the paper.
- Paper V:** The author conducted the experimental work. The wear tests were performed at CIDETEC. The author wrote the first draft of the paper.
- Paper VI:** The author conducted the microscopy work, i.e. SEM and EBSD analyses. The results were analysed and discussed with all co-authors. The paper was written in collaboration with the co-authors.
- Paper VII:** The author planned the work and conducted the annealing treatments and the microstructural analysis. The nanoindentation measurements were performed at the Department de Física of the Universitat Autònoma de Barcelona by Dr. Jordina Fornell. The wear tests were performed at CIDETEC by Dr. Naroa Imaz. The author wrote the first draft of the paper.

### Papers not appended to the thesis

- Alkoxyated  $\beta$ -Naphthol as an Additive for Tin Plating from Chloride and Methane Sulfonic Acid Electrolytes  
S. P. Zajkoska, A. Mulone, W. E. G. Hansal, U. Klement, R. Mann, W. Kautek  
*Coatings, Volume 8(2), Page 79, 2018.*
- Development of advanced hybrid materials with the help of pulse electrodeposition  
U. Klement, N. Mortazavi, A. Mulone, D. Melciu & N. Maidee  
*Transactions of the Institute of Metal Finishing, Volume 93(6), Pages 296–301, 2015.*
- Thermal stability of white layers intended as process-induced functional coatings  
U. Klement, A. Mulone, S. Hosseini  
Paper in *Proceedings of the 12<sup>th</sup> Asia-Pacific Microscopy Conference, 3-7 February 2020, Hyderabad, India.*



## Table of Contents

1	Introduction.....	1
1.1	Electrodeposition with an environmentally friendly approach.....	2
1.2	Objective and Research Questions .....	4
1.3	Research approach and limitations .....	5
2	Background .....	7
2.1	Electrodeposition: the set up and basic principles .....	7
2.2	Electrodeposition of single metals and alloys .....	8
2.3	Electrocrystallization steps and electrodeposit microstructures .....	9
2.4	Nanocrystalline and amorphous electrodeposits .....	12
3	Electrodeposited Fe-W alloys and deposition methods .....	15
3.1	Previous studies on electrodeposited Fe-W alloys .....	15
3.2	Electrodeposition of Fe-W and Fe-W/Al <sub>2</sub> O <sub>3</sub> coatings: electrolyte and coatings composition .....	16
4	Characterization techniques .....	19
4.1	Imaging techniques.....	19
4.1.1	Optical microscopy .....	19
4.1.2	Scanning electron microscopy (SEM).....	19
4.1.3	Electron back scatter diffraction (EBSD).....	20
4.1.4	Transmission electron microscopy (TEM).....	22
4.2	Non-imaging techniques.....	23
4.2.1	X-ray diffraction (XRD).....	23
4.2.2	Glow discharge optical emission spectroscopy (GD-OES) .....	24
4.2.3	Heat treatments.....	24
4.2.4	Differential scanning calorimetry (DSC) .....	24
4.2.5	Nanohardness measurements .....	25
4.2.6	Ball-on-disc measurements .....	26
4.2.7	Potentiodynamic measurements and electrochemical impedance spectroscopy .....	26
5	Summary of results and discussions .....	29
5.1	Interdependences between the composition, the structure and the thermal stability of Fe-W coatings.....	29
5.2	Heat treatment effects on the hardness and elastic modulus of Fe-W coatings .....	33
5.3	Wear resistance of as-deposited and annealed Fe-24W coatings .....	35
5.4	Wear and corrosion resistance of Fe-W/Al <sub>2</sub> O <sub>3</sub> composites .....	37
5.5	Mechanical and wear properties of annealed Fe-W/12%Al <sub>2</sub> O <sub>3</sub> composites.....	40

6	Conclusions.....	43
7	Future work.....	47
8	Acknowledgements.....	49
9	References.....	51

## 1 Introduction

Electrodeposition is a wet-chemical process which through the electrochemical reduction of metal ions from an electrolyte results in the deposition of a metallic coating onto a base material. The first large-scale industrial plant for electrodeposition was built in the 19<sup>th</sup> century for the deposition of gold, silver and copper for decorative applications [1]. Since then, electrodeposition has rapidly grown and it has been applied for the deposition of metals, alloys and composites with complex shapes (i.e. coatings, micropillars, nanowires) and to produce dense nanostructures and amorphous coatings with increased mechanical, corrosion, electrical and magnetic properties [2,3]. Thanks to this progress, today, electrodeposition is a widely employed technique for the production of coatings ranging from decorative to technological applications. According to a recent survey, electrodeposition dominates the metal finishing market with around 40% of the share [4], particularly for the electrodeposition of nickel, zinc and chromium coatings [5] as protective and/or decorative coatings in the automotive and aerospace industry [6–8]. Furthermore, electrodeposition applied in the field of microelectronic devices, energy conversion and bio-electrochemistry represents an area of extensive research and innovation [9–11].

Compared to various deposition techniques electrodeposition offers several advantages, e.g. its relative simplicity of implementation, the low capital cost needed, and the high process versatility. Electrodeposition processes are usually performed with aqueous-based electrolytes, at ambient pressure, and low operating temperatures (i.e. lower than 100 °C). Furthermore, owing to an increased understanding of the electrodeposition fundamentals, with a proper control of the deposition parameters, it is possible to fine-tune the material characteristics (e.g. composition and microstructure) and consequently the material properties.

However, one of the main drawbacks of electrodeposition is the environmental impact and the health risk associated with the electrolyte composition. Many electroplating processes involve the use of highly corrosive solutions, toxic chemicals and compounds. For example, the electrodeposition of hard chromium coatings involves the use of highly cancerogenic compounds (i.e. hexavalent chromium) [12,13]. The health risk associated with the exposure to toxic compounds used in the electrodeposition industries (e.g. Cd, Pb, and Cr<sup>6+</sup>) is not limited to the workers. In fact, part of the electrolytes used in electrodeposition processes ends up as wastewater [14]. To limit these risks, strict environmental regulations are implemented in the European Union. For example, the use of hexavalent chromium, lead and cadmium has been restricted since 2003 (DIRECTIVE 2002/95/EC) [15].

The integration of environmental and sustainability concerns into technological progress remains a significant challenge for our modern society. The 17 UN goals for a sustainable development represent a constant reminder of what to achieve for a better and more sustainable future [16], see Fig. 1. In the field of industrial manufacturing and material science, the main goal to relate to is *Goal 12* (i.e. Responsible consumption and production) together with its sub-goals (e.g. Management of natural resources, Management of chemical waste, Recycling etc.). However, in a broader view, it is not hard to imagine that obtained achievements with respect of sustainable production would have an important role also on other UN goals, e.g. *Goal 6* (i.e. Clean water and sanitation), and *Goal 9* (i.e. Industries, innovation and infrastructure). Hence, to face these issues in the field of electroplating industry, it is of major importance to move toward sustainable alternatives for coatings produced using environmentally hazardous

processes. It would benefit both the environment and the electrodeposition industrial market, the growth of which is limited by the environmental regulations [4].



Figure 1. The 17 UN goals for a sustainable development. The image does not require prior permission from the United Nations nor the conclusion of a licensing agreement [17].

## 1.1 Electrodeposition with an environmentally friendly approach

On December 18<sup>th</sup> 2006, the European Union regulation REACH (Registration, Evaluation, Authorization and Restriction of Chemicals) was launched [18]. The aim of REACH is to address the production and use of chemical substances and their impact on both environment and human health. With the help of ECHA (European Chemicals Agency), formed in 2007 as administrative body of REACH, the first list of Substances of Very High Concern (SVHC) was published in 2008 and since then it is regularly updated with new candidates [19]. The inclusion of a compound in the list of SVHC is the first step in the procedure for strict regulations and restrictions for its use. If a chemical from the SVHC list is also included in the Annex XIV of REACH, it is given a latest application date referred as "sunset date" [20]. After the sunset date, the material is not supposed to be used anymore. However, the European Commission can still authorize the import and the use of the substance under very strict rules and only for a limited period.

Since compounds containing hexavalent chromium are listed in Annex XIV, many studies have been conducted with the aim to find an environmentally friendly alternative to electrodeposited hard chromium coatings. Trivalent chromium plating (i.e.  $\text{Cr}^{3+}$ ) is less harmful and it is considered a promising technology. But its application is still limited due to the achievable thickness and surface quality issues of the obtained chromium coatings [21]. Electrodeposited Co and Ni-based alloys with additions of W and/or P have been proposed as a replacement to hard chromium because of their excellent corrosion resistance and mechanical properties [22–27]. The co-deposition of W and/or P affects the microstructure of the coatings, which results in enhanced properties. However, Ni and Co-based coatings do not represent a valid

environmentally friendly alternative. Cobalt salts are also included in the list of SVHC as a cancerogenic compound. The use of Ni is discouraged because it is highly allergenic (EN 16128:2011) and the inhalation during the manufacturing process may lead to respiratory diseases and increases the risk of carcinogenicity [28,29]. Phosphorous is widely used in agriculture, being an essential and non-replaceable nutrient for plants and animals. Since 2013, the European Commission has therefore launched a consultation on how to use phosphorous in a more sustainable way [30]. Thus, the attempt to find an environmentally friendly alternative to hard chromium coatings is still under investigation.

The importance to consider sustainability issues in the field of electrodeposition is discussed in Paper I. In the paper it is proposed a sustainable approach aiming to provide guidelines for the research applied in finding alternatives to coatings produced with hazardous processes and using scarce and non-renewable resources. The suggested sustainable approach can be summarized with the following steps:

1. **Material selection:** Avoid or minimize using raw-materials compounds listed as critical raw material (CRM).
2. **Electrolyte design:** Avoid using compounds listed as SVHC, especially if included in restriction and authorizations lists of REACH.
3. **Life cycle:** Consider the recyclability of the used compounds. When using CRM, an efficient recycling can help in mitigating the environmental impact of the product.

Between the three sustainable steps, step 2 and 3 are of particular importance. Avoiding the use of CRMs is certainly beneficial for the sustainability of the product. However, the complete replacement of CRM can cause some disadvantages such as the possibility of degrading the product properties [31]. Furthermore, the complete replacement of a CRM with a certain substitute might result in increasing the economic importance and supply risk of the substitute, which consequently might be shifted into criticality [32]. Hence, the efficient recycling of CRMs represents a solution to alleviate the replacement of CRMs. Improvements in the recycling of CRM are although required, since the recycling rates of CRM are still extremely low (e.g. 0.0% for Co and 8.0% for heavy rare earth metal) [33]. When comparing the low recycling rates of CRMs, tungsten and vanadium represent an exception with recycling rates above 40%.

Among the electrodeposited alloys proposed as a sustainable replacement of hard chromium coatings, Fe-based alloys have not been extensively studied as compared to Co and Ni-based coatings. Yet, iron is one of the most abundant elements and the production of its alloys could be in accordance with environmental concerns. Hence, in consideration of the sustainable approach discussed above, this research work comprises the study of Fe-W deposited alloys using a properly developed electrolytic bath, i.e. minimally invasive, thermodynamically stable, and without toxic compounds, as those listed as SVHC.

## 1.2 Objective and Research Questions

This thesis work focuses on electrodeposited Fe-W and Fe-W/Al<sub>2</sub>O<sub>3</sub> composite coatings, designed and deposited in consideration of the sustainability constraints previously introduced. Such coatings aim to be applied as a sustainable alternative to hard chromium coatings, therefore the mechanical properties (i.e. hardness and elastic modulus) and the wear and corrosion resistance of the Fe-W alloys are studied. The objective of this thesis is to evaluate the interdependencies between the material characteristics (e.g. composition and structure) and the properties of interest, concentrating on the mechanical properties and wear resistance. The results aim to provide useful information on how to tailor and control the microstructure of the material and consequently the material properties.

The objective of the work can be divided into the following research questions:

- RQ1: How is the composition (i.e. the W content) influencing the structure and the thermal stability of Fe-W coatings?
- RQ2: How are composition and structure influencing the hardness of Fe-W coatings?
- RQ3: What is the main factor determining the wear and corrosion resistance of Fe-W coatings? Can such properties be improved with the co-deposition of hard particles such as Al<sub>2</sub>O<sub>3</sub>?
- RQ4: Which combination of material characteristics and annealing treatments results in optimum hardness and wear resistance in Fe-W alloys? Are such properties comparable to the hardness and wear resistance of hard Cr coatings?

### 1.3 Research approach and limitations

To answer the research questions, this thesis work was performed by following a research approach as described in Fig. 2. The different steps of the applied research approach can be described as follows:

1. Design of an environmentally friendly electrolyte and the electrodeposition of Fe-W coatings with various W contents.
2. Detailed structural characterization of the as-deposited and annealed Fe-W coatings. The results are presented in Paper II.
3. Study of the mechanical properties of the Fe-W coatings and how such properties are influenced by the structure and composition. In-situ TEM annealing experiments are performed to provide further understanding of the interdependencies between the microstructure and mechanical properties observed upon annealing. The results are presented in Paper III and Paper IV.
4. Study of the wear resistance of as-deposited and annealed Fe-24at.%W coatings. The analysis of wear resistance was limited to W-rich coatings in consideration of the previously acquired results. The possibility to improve the coating's wear and corrosion resistance was investigated by co-depositing alumina particles in various amounts. The results are presented in Paper V and Paper VI.
5. Heat treatments of Fe-W/12%Al<sub>2</sub>O<sub>3</sub> coatings are performed in order to optimize the hardness and wear resistance of the composite coating. The study was limited to Fe-W/12%Al<sub>2</sub>O<sub>3</sub> composites in consideration of the previously acquired results. The properties of the composite coatings are compared to the hardness and wear resistance of electrodeposited hard Cr coatings. The results are presented in Paper VII.

This research work has focused on the characterization of the microstructure and properties of electrodeposited Fe-W alloys. The design of the electrolytic bath and the deposition of the coatings (step 1) was performed by a collaborator (Dr. Nicolenco, who was at that time a PhD student at Vilnius University and involved in the H2020-MSCA-ITN SELECTA project). The parameters applied for the deposition of the Fe-W and Fe-W/Al<sub>2</sub>O<sub>3</sub> coatings are included in the thesis and in the appended papers. However, this work is not aiming at investigating the influence of the deposition parameters on the thermodynamics of the electrochemical deposition process. Hence, a detailed discussion of the design and characterization of the electrolytic bath, and on the optimization of the applied deposition parameters is not provided.

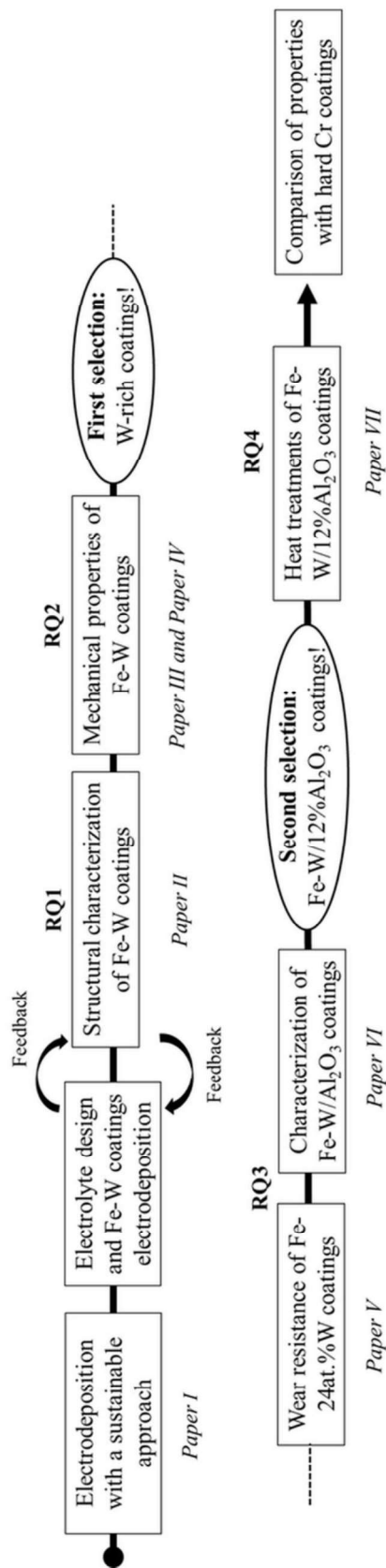


Figure 2. Schematic illustration of the applied research approach.

## 2 Background

In this chapter, a brief overview of the electrodeposition process including the electrodeposition set up and some of the electrodeposition fundamental concepts are provided. Also, the concept of electrocrystallization and of nanocrystalline and amorphous electrodeposits are introduced.

### 2.1 Electrodeposition: the set up and basic principles

The necessary components for an electrodeposition set up are the following: (i) an electrolyte (often aqueous-based) containing the ions of the material to be deposited, (ii) an external power supply (i.e. current or potential difference), which is connected to (iii) the working electrode (the substrate to be coated) and to (iv) the counter electrode. The described set up is shown in a schematic representation in Fig. 3. The working electrode is connected to the negative terminal of the power supply. In this way, the metal ions dissolved in the electrolyte are first attracted in the proximity of the working electrode surface, and then reduced to metal atoms. With time, this process will result in the formation of a coating on the surface of the working electrode.

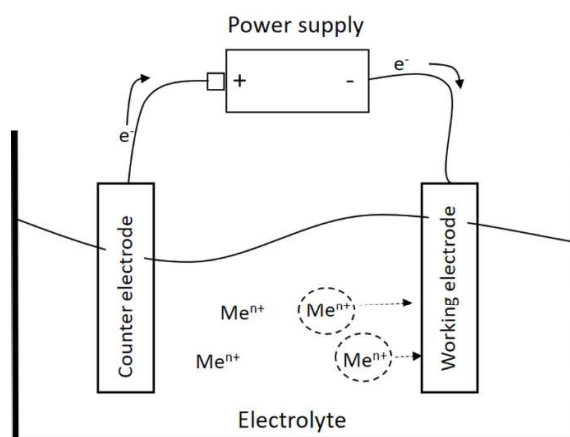


Figure 3. Schematic representation of the setup for an electrodeposition process. In the graph  $Me^{n+}$  stands for the metallic cation dissolved in the electrolyte.

The relationship between the applied current and the amount of deposited material is described by Faraday's law [34]:

$$m = QA/nF$$

where  $m$  is the mass of the deposited metal,  $Q$  is the net charge applied to the system,  $A$  is the atomic weight of the metal,  $n$  the number of electrons transferred during the deposition process, and  $F$  is the Faraday constant. With the assumption of applying a constant current (i.e.  $Q = I\tau$ , where  $I$  is the current and  $\tau$  the duration of the electrodeposition), Faraday's law can be expressed as the dependence of the coating thickness  $h$  ( $h = m/Sd$ , where  $S$  is the surface area and  $d$  is the density) upon the duration of the electrodeposition,  $\tau$ , and the applied current density,  $j$  (where  $j=I/S$ ):

$$h = jAt/ndF$$

During an electrodeposition process, part of the applied current is often consumed by side reactions (e.g. hydrogen evolution) occurring in parallel with the metal deposition. To consider the effect of such side reactions, the current efficiency (CE) of a certain deposition process is defined as the ratio of the actual deposited mass,  $\Delta m$ , with respect of the theoretical value as calculated from Faraday's law:

$$CE = \Delta m / (QA/nF)$$

The electrodeposition of metals and alloys is commonly performed using an aqueous-based solution as electrolyte. In its most simple form, an electrolyte contains salts or other soluble compounds containing the metal of interest. However, electrolytes containing exclusively one component are rarely used in practice since they do not provide high quality coatings. Complexing agents, i.e. typically organic acids, are often added to stabilize the metal complexes of interest and to increase the conductivity of the solution. Buffering agents (e.g. boric acid or ammonia) can be added to stabilize the pH of the electrolyte. Also, different organic substances known as additives can be added to the electrolyte for various reasons. Among the most commonly employed additives there are: (i) surfactants, added to decrease the surface energy of the working electrode, (ii) grain-refiners, added to make the deposited metal surface smooth, (iii) brighteners, added to obtain a bright finish deposit, and (iv) levelers, added to fill pre-existing scratches or voids in the surface of the electrode. These additives are often included in the electrolyte to hinder the cathodic process, i.e. the reduction of the metal cations. The hindering of the cathodic process occurs through the physical/chemical absorption of the additives into the surface active sites of the electrode [35].

## 2.2 Electrodeposition of single metals and alloys

In order to study the different phenomena occurring during an electrodeposition process, i.e. reaction mechanism of metal deposition, hydrogen evolution, or the effects of the additives, polarization measurements are commonly performed. A polarization curve describes the relationship between the potential and the current during an electrochemical reaction. A polarization curve is obtained by varying the applied potential and by measuring the corresponding value of the current. To perform such a measurement, a three-electrode set up is needed, which includes a reference electrode. In fact, the applied potential to drive the electrochemical reaction is measured with respect to the reference electrode. Figure 4 shows a schematic representation of a three-electrode set up and a representative polarization measurement for the electrodeposition of Sn from a chloride-based electrolyte. In Fig. 4b, the curve shown with the continuous line is measured in the electrolyte without additive, the curve shown with the dashed line is measured after adding 3.12 mg/l of  $\beta$ -Naphthol (referred as ABN in the graph) [36]. In both polarization curves in Fig. 4b, the measured cathodic current density increases rapidly at a potential around -700 mV, until a plateau is reached. The increase in current density is associated with the diffusion-limited reduction of  $\text{Sn}^{2+}$  into metallic Sn. After the plateau, a rapid increase in the current density is observed for the Sn electrodeposition without the addition of the additive. This is due to hydrogen evolution. As observable from the dashed curve, the additive leads to a decrease of the measured cathodic current density and to a suppression of the hydrogen evolution. These effects are typical of additives providing inhibition during the performed electrodeposition.

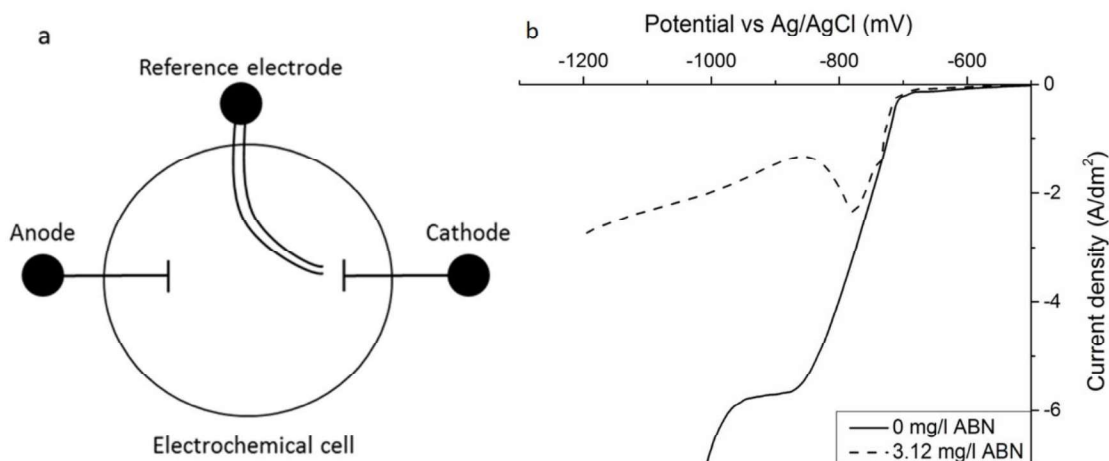


Figure 4. Schematic representation of a three-electrode set up (a), and polarization curves measured for the electrodeposition of Sn from a chloride-based electrolyte (b). The curve with the continuous line is measured in the electrolyte without additive, the curve with the dashed line is measured after adding 3.12 mg/l of ABN.

The electrodeposition of alloys is a more complex process as compared to the deposition of a single metal. To deposit alloys, a stringent control of the electrolyte composition, deposition condition and parameters (e.g. applied current density or potential) is required. Usually, the deposition of a single metal can occur within a potential window of 0.2-0.3 Volts, regardless of the type of electrolyte and other deposition conditions applied [34]. Hence, for two metals to be deposited simultaneously, it is necessary that the potential ranges for deposition of the individual metals overlap. Only few metal pairs are characterized with sufficiently close reduction potentials when deposited from solutions of their simple salts. Different approaches can be applied to reduce the difference between the reduction potentials of the metals of interest. Among the possible approaches, adding complexing agents into the solution is usually done to reduce the gap between the deposition potentials. Common complexing agents are cyanides, ammoniates, pyrophosphate and other organic acids like citrates and gluconates. Complexing agents are also used when depositing elements that cannot be reduced by themselves in an aqueous electrolyte, e.g. W and Mo. The deposition of such elements can only be induced through the deposition of another element, resulting in the formation of an alloy. Due to this peculiarity, such mechanism was defined as *induced co-deposition* by Brenner in the 1940s [37]. Since this study, the induced co-deposition of W and Mo alloys with iron group metals (i.e. Ni, Co and Fe) has been extensively investigated, but the reaction mechanisms are still not well understood.

### 2.3 Electrocrystallization steps and electrodeposit microstructures

When depositing metallic coatings, all the possible electrodeposition processes have in common the transfer of one or more electrons through the electrode/solution interface. The overall deposition process can be divided in three main steps [34] and Fig. 5 provides a schematic representation of the three steps. The first step is represented by the mass transfer of the metallic cation to the surface of the working electrode. The second step involves the charge transfer

between cation and working electrode, and the adsorption of the reduced metal atom at the surface of the electrode. In the last step, the adsorbed metal atom can diffuse to an active growth site in the surface, i.e. a surface defect such as a kink site or an atomic step (see  $C_1$  and  $C_2$  in Fig. 5) [38]. The diffusion of the adions to active sites occurs because the adions are more stably bound to the substrate at such sites. In fact, after the charge transfer (step 2 in Fig. 5) the adsorbed adion is neither completely discharged nor completely de-solvated [38]. It still carries ligands with a negative charge (e.g. complexing species) from the electrolyte. When an adion occupies a step or kink position, it is less hydrated than a corresponding adion adsorbed at a free-surface site. Hence, the bonding to the substrate in a step and in a kink site is stronger.

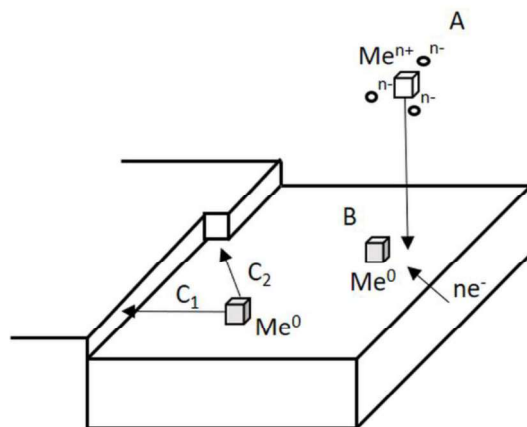


*Figure 5. Schematic illustration of the three main steps of an electrocrystallization process: mass transfer of the active species (A), charge transfer between adion and the substrate (B), diffusion of adion to an active growth site like an atomic step ( $C_1$ ) or a kink site ( $C_2$ ). In step A, the particles with the negative charge are representing ligands from the electrolyte.*

The growth of the electrodeposited metal or alloy can proceed according to different models [34]. In the case of electrodeposition occurring at a surface with a high density of active sites (i.e. kink and step sites) and with low inhibition (e.g. using an electrolyte without or with low amounts of additives), the discharge and attachment of atoms to the lattice occurs across the whole surface. This leads to the formation of isolated “island” nuclei which will afterwards grow vertically. This is known as the “Volmer-Weber” island growth mode [39]. Often, the deposited layer obtained from such growth mode is weakly attached to the substrate and is associated with a rough surface. The “Stransky-Krastanov” growth mode (island growth on top of pre-deposited monolayers) occurs when using additives providing moderate inhibition. As discussed in the previous paragraph, the additives adsorb on the active sites thus forcing the metal ions to be reduced in the atomic planes rather than steps and kinks. An initial later growth of the film is obtained forming a monolayer where, as the deposited layer builds up, island nuclei will form and grow. When a stronger inhibition is applied during the electrodeposition, the “Frank-van der Merwe” layer-by-layer growth is obtained which results into smooth and fine grained deposits [39]. Depending on the growth mode of the electrodeposited film, different microstructures can be formed. A classification of the different microstructures commonly encountered was provided by Fisher [40] and then re-proposed by Winand [41]:

1. field-oriented isolated crystals type (FI)
2. basis-oriented reproduction type (BR)
3. twinning intermediate type (Z)
4. field-oriented texture type (FT)
5. unoriented dispersion type (UD).

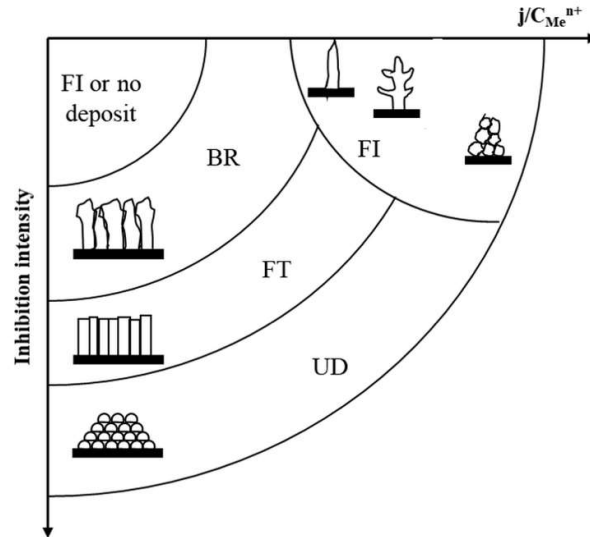


Figure 6. Diagram showing the different microstructures commonly found in electrodeposits as a function of the inhibition intensity and the ratio between current density and the concentration of the metal ions ( $j/C_{Me}^{n+}$ ). Adapted from [41].

Figure 6 shows a schematic illustration of the different microstructure types as a function of the inhibition intensity and the ratio between the current density and the concentration of metal ions,  $j/C_{Me}^{n+}$ , as proposed by Winand [41]. As shown in Fig. 6, the FI microstructure is occurring at low inhibition, and by increasing the current density, unstable film structures will be formed, such as whiskers, dendrites and powder deposits. The BR type is obtained with moderate inhibition promoting an initial lateral growth of the film. The lateral growth is then followed by the formation of larger crystals and by the possible degradation from BR type to FI type structure. At quite strong inhibition, the FT type is obtained, which is characterized by the formation of elongated crystals growing perpendicular to the substrate. The UD type is obtained at even higher inhibition, leading to the formation of a coherent deposit with randomly arranged fine grains. As described by Fischer [41], the twinning intermediate type (Z) is a transitional microstructure from the BR to the FT type. In the schematic drawing shown in Fig. 6, the twinning intermediate microstructure (Z) is not included.

The peculiar microstructures observed in electrodeposited coatings, together with the co-deposited impurities within the coatings, are the main reason why the physical, chemical and mechanical properties of electrodeposited metals and alloys usually differ from the properties of the pure metallurgical samples [34]. In fact, in an electrochemical environment the nucleation and growth process deviate strongly from equilibrium conditions, due to the large driving force for the electrocrystallization (i.e. current density or potential). Hence, the resulting microstructure is metastable and contains a high concentration of structural defects (i.e. grain boundaries, twin boundaries and dislocations). The presence of co-deposited impurities (e.g. O,

C and H) can also be related to the electrodeposition process. For example, carbon is often found in coatings deposited from baths containing additives and/or complexing agents. The precipitation and co-deposition of hydroxide compounds can be observed when the pH at the electrode/solution interface is sufficiently high to cause metal hydrolysis in the vicinity of the cathode. Finally, hydrogen is often formed as a side reaction during electrodeposition.

## 2.4 Nanocrystalline and amorphous electrodeposits

As mentioned in the previous chapter, the electrocrystallization of a metal occurs far from equilibrium conditions which often results in a microstructure characterized with a large volume fraction of grain boundaries. A large volume fraction of grain boundaries is in turn associated with small grain sizes. Hence, electrodeposition can be considered as a grain boundary engineering process which allows to control the volume fraction of grain boundaries during the deposition of the material [42]. In Fig. 7, a schematic representation of the volume fraction of grain boundaries and total intercrystalline region as a function of grain size is shown. For the calculation of the total intercrystalline volume fraction, Palumbo et al. [43] assumed a 14-sided tetrakaidekahedron as grain shape, and a grain boundary thickness ( $\Delta$ ) of 1 nm. As shown in Fig. 7, when the grain size is reduced below 100 nm, both the grain boundary fraction and the intercrystalline volume fraction begins to account for a significant volume fraction of the material (~50% at a few nm in grain size, as marked in Fig. 7).

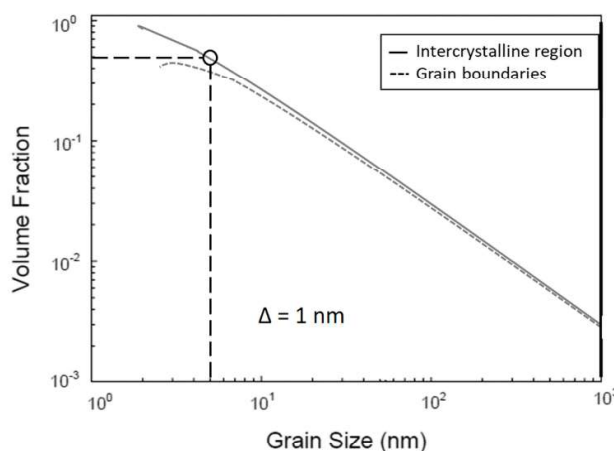


Figure 7. The effect of grain size on the volume fractions of intercrystalline regions and grain boundaries, assuming a grain boundary thickness,  $\Delta$ , of 1 nm. Image adapted from [43].

The first studies on the electrodeposition of nanocrystalline materials were published in the late 1980s [44]. Since then, the interest for the electrodeposition of nanocrystalline materials has rapidly grown, and the deposited coatings have been applied in several commercial applications [3]. In fact, several materials properties are affected by a grain size refinement. Mechanical properties, e.g. hardness and yield strength, and the wear resistance have shown to considerably increase with decreasing the material grain size [42], see Fig. 8.

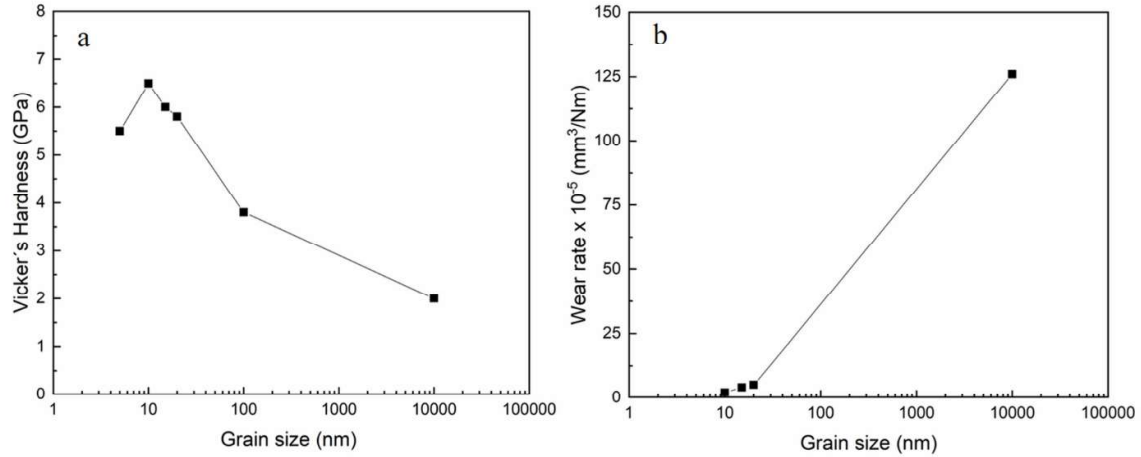


Figure 8. The effect of grain size on the hardness and wear rate on electrodeposited Ni coatings. Image adapted from [42].

The substantial increase in hardness observed in Fig. 8 can be related to the Hall-Petch equation describing the relationship between strength and grain size in a polycrystalline metal:

$$\sigma_y = \sigma_0 + \frac{k_y}{\sqrt{d}}$$

Where  $\sigma_y$  is the yield strength,  $\sigma_0$  is the minimum stress required for dislocation motion in the absence of grain boundaries,  $k$  is a constant and  $d$  is the grain size. As described by the Hall-Petch relation, the strength and hardness (i.e.  $H \propto \sigma_y$ ) of a polycrystalline metal increases by decreasing its grain size ( $d$ ). As shown in Fig. 7, by decreasing the grain size the number of grain boundaries within a material increases. The grain boundaries constrain the motion of dislocations resulting in a strengthening of the material. The Hall-Petch trend of the strength as a function of inverse root square of the grain size is empirically accepted for grain size larger than  $\sim 20$  nm. For grain sizes below  $\sim 20$  nm, the hardness variation exhibits a plateau or even a reduction in hardness (as can also be observed in Fig. 8a). Such phenomenon is referred to as the Hall-Petch break-down or the inverse Hall-Petch effect [45]. The critical grain size for the Hall-Petch break-down can vary depending on the analysed metal. For example, for pure electrodeposited nickel, researcher have suggested that the Hall-Petch breakdown occurs at  $\sim 15$  nm [46]. However, studies on electrodeposited Ni-W coatings have shown that alloying with W can cause a suppression of the breakdown resulting in smaller critical grain size, i.e.  $d \sim 7$  nm [47].

Electrodeposition can also be applied to deposit amorphous alloys, i.e. materials with a glass-like structure with no long-range ordering. Amorphous alloys are usually formed by the co-deposition of non-metallic elements (e.g. boron, phosphorous, sulphur, oxides and hydroxides) or refractory metals, e.g. tungsten [34]. When deposited in sufficiently high amount (i.e. at least 15 at.%), these components act as amorphizing additives and inhibit the crystallization process. In fact, the addition of these components leads to a drastic decrease in the diffusion rate of the elements in the system. An amorphous structure largely influences the material properties. Amorphous materials are often characterized with high yield strength, hardness and elastic strain, which make them attractive for various structural applications [48,49]. Also, due to the absence of structural defects such as grain boundaries and dislocations, amorphous materials

can exhibit high corrosion resistance [50]. However, the lack of dislocations and slip systems results also in low tensile ductility, causing a brittle failure of the amorphous materials upon yield [48].

As a result of their enhanced mechanical and wear properties, nanocrystalline and amorphous alloys are of great interest for protective coating applications. However, due to their peculiar structure, nanocrystalline and amorphous materials are in a metastable state. There is a strong driving force for grain growth and crystallization of stable phases with increasing the temperature. Hence, the thermal stability of these materials can be rather low.

### 3 Electrodeposited Fe-W alloys and deposition methods

In this chapter, the investigated electrodeposited Fe-W alloys are presented. First, previous studies on the electrodeposition of Fe-W alloys are summarized, afterwards the deposition parameters applied for the deposition of the Fe-W and Fe-W/Al<sub>2</sub>O<sub>3</sub> coatings are discussed.

#### 3.1 Previous studies on electrodeposited Fe-W alloys

As mentioned earlier (paragraph 2.2), pure W cannot be deposited by itself from aqueous electrolytes but only through the deposition of another element. The first studies on the co-deposition of W with iron group metals (i.e. Fe, Ni and Co) are found between the 1930s-1940s [37,51,52], but the mechanism of W co-deposition is still studied today [53,54]. The structure of the electrodeposited metal is strongly influenced by the amount of co-deposition of W. An increase in the W content is often associated to a transition from a nanocrystalline to an amorphous structure [55]. In the case of Fe-W coatings, a nanocrystalline solid solution is formed in Fe-W coatings deposited with relative low W content. The deposited alloy retains the structure of the base metal (bcc-iron), with an increased lattice parameter as compared to pure iron [55]. A mixed amorphous-crystalline structure has been observed for W contents ranging between 11 and 20 at.% [56], whereas a homogeneous amorphous structure is usually obtained for W contents higher than 20 at.% [57,58]. Tungsten addition and the associated structural changes lead to an improvement in the chemical, mechanical, tribological and magnetic properties of the electrodeposited alloy. Among electrodeposited W-containing alloys, recent studies have mainly focused on the improvement of the corrosion resistance, and of mechanical and tribological properties of Ni-based [59–65] and Co-based alloys [66–71]. Regarding Fe-W alloys, fewer studies are found and they have mainly focused on the hardness and wear properties [72–74], on the thermal stability and corrosion resistance [58,75], or on magnetic properties [76,77]. However, the effect of heat treatments on the mechanical and tribological properties of Fe-W alloys has been overlooked.

Since the first studies on the electrodeposition of Fe-W alloys, the electrolytes used for the deposition have changed over the years. Such alloys can be deposited from solutions based either on Fe(II) or Fe(III) metallic salts (i.e. sulphates or chlorides). Simple Fe(II)-based solutions tend to easily oxidize (i.e. the dissolved Fe<sup>2+</sup> ions will oxidize to Fe<sup>3+</sup> ions), which causes the destabilization of the bath. Hence, electrolytes containing complexing agents, such as citates and ammonia, which are added to hinder the Fe(II) oxidation process have been extensively studied [78–80]. However, the Fe(II) oxidation is inhibited but not fully prevented [6]. The stability of Fe(III)-based electrolytes is challenged by the hydrolysis of the Fe<sup>3+</sup> ions. Thus, the overall bath stability is determined by the competing reactions of the Fe<sup>3+</sup> ion hydrolysis and the stability of its complexes. The deposition from Fe(III) solutions can be characterized with rather low current efficiency and the obtained coatings have a lower W content as compared to the alloys deposited from Fe(II) electrolytes (the current efficiency for Fe-W electrodeposition generally does not exceed 50% [81]). Thus, fewer studies have investigated Fe(III)-based electrolytes [77,82,83].

The Fe-W alloys studied in this thesis work have been deposited from an environmentally friendly Fe(III)-based glycolate-citrate electrolyte recently developed by Dr. Nicolenco. From this bath, by changing the deposition parameters (i.e. pH, temperature and current density), Fe-W coatings can be deposited with tungsten contents varying from a few at.% to 25 at.%, and

with current efficiencies up to 60-70% [81,84]. The achieved current efficiency represents a substantial improvement in the lifetime of the electrolyte and thus on its environmental impact.

### 3.2 Electrodeposition of Fe-W and Fe-W/Al<sub>2</sub>O<sub>3</sub> coatings: electrolyte and coatings composition

Fe-W and Fe-W/Al<sub>2</sub>O<sub>3</sub> coatings were deposited from a glycolate-citrate plating electrolyte with the following composition: 1 M glycolic acid, 0.3 M citric acid, 0.1 M (Fe)<sub>2</sub>(SO<sub>4</sub>)<sub>3</sub> and 0.3 M Na<sub>2</sub>WO<sub>4</sub>. The deposition was performed in a typical three-electrode cell characterized by (i) a copper or brass sheet as working electrode (i.e. the substrate), (ii) a platinized titanium mesh as counter electrode and (iii) a saturated Ag/AgCl/KCl as reference electrode. Before the electrodeposition of the coatings, the substrates were degreased using acetone and ethanol and activated in a 2 M H<sub>2</sub>SO<sub>4</sub> solution for 1 minute. Finally, for the deposition of the Fe-W/Al<sub>2</sub>O<sub>3</sub> composite coatings, a Ni-seed layer was deposited from a commercial chloride bath applying 30 mA/cm<sup>2</sup> at 65 °C for 1 minute to improve the adhesion with the brass substrate. This thesis has focused on the characterization of Fe-W coatings with three different W contents: 4, 16 and 24 at.% of W. The applied deposition parameters are specified in Table 1, together with the chemical compositions measured by EDS analyses along the cross-section of the coatings. The sample code specified in Table 1, i.e. Fe-4W, Fe-16W and Fe-24W will be used in the following text.

Table 1. Deposition parameters and EDS chemical composition of Fe-W coatings.

Sample code	T (°C)	pH	J (mAcm <sup>-2</sup> )	CE(%)	Composition (at.%)	
					Fe	W
Fe-4W	20	6.5	15	24	96	4
Fe-16W	65	5	15	50	84	16
Fe-24W	65	6.5	15	72	76	24

Due to the limitations of EDS in quantifying light elements (e.g. O, C and H), the composition of the coatings is presented as content of the metallic phase only, i.e. Fe and W. GD-OES measurements were performed to get a reliable quantification of the co-deposited impurities. As shown by GD-OES results (Paper II), co-deposited O and C are mainly found at the surface of the coatings, and the amount of such impurities decreases rapidly within the first 0.5-0.7 μm. With increasing the amount of deposited W in the coating, a decrease in the amount of co-deposited O can be observed. In particular, the co-deposited oxygen decreases from ~7 at.% to less than 1 at.% when comparing Fe-4W and Fe-24W.

For the deposition of Fe-W/Al<sub>2</sub>O<sub>3</sub> coatings, sub-microsized alumina particles (Alfa Aesar 42572) were added to the electrolyte with the concentration of 25, 50, and 100 g l<sup>-1</sup>. Prior to the electrodeposition of the composites, the suspensions were stirred at 300 rpm for 24 h, plus ultrasonically agitated for 10 minutes to avoid the agglomeration of the particles. The electrodeposition was performed with a constant cathodic current density of 40 mAcm<sup>-2</sup>, with a bath temperature of 65 °C, and by applying a stirring rate of 200 rpm. The applied parameters resulted in the deposition of a composite containing ~ 3, 6 and 12vol.% of alumina particles (as measured by image analysis, Paper V). Hence, in the following text the composite coatings will be addressed as Fe-W/3%Al<sub>2</sub>O<sub>3</sub>, Fe-W/6%Al<sub>2</sub>O<sub>3</sub> and Fe-W/12%Al<sub>2</sub>O<sub>3</sub>.

The surface morphology and the cross-section of the studied Fe-W alloys are shown in the SEM micrograph in Fig. 9.

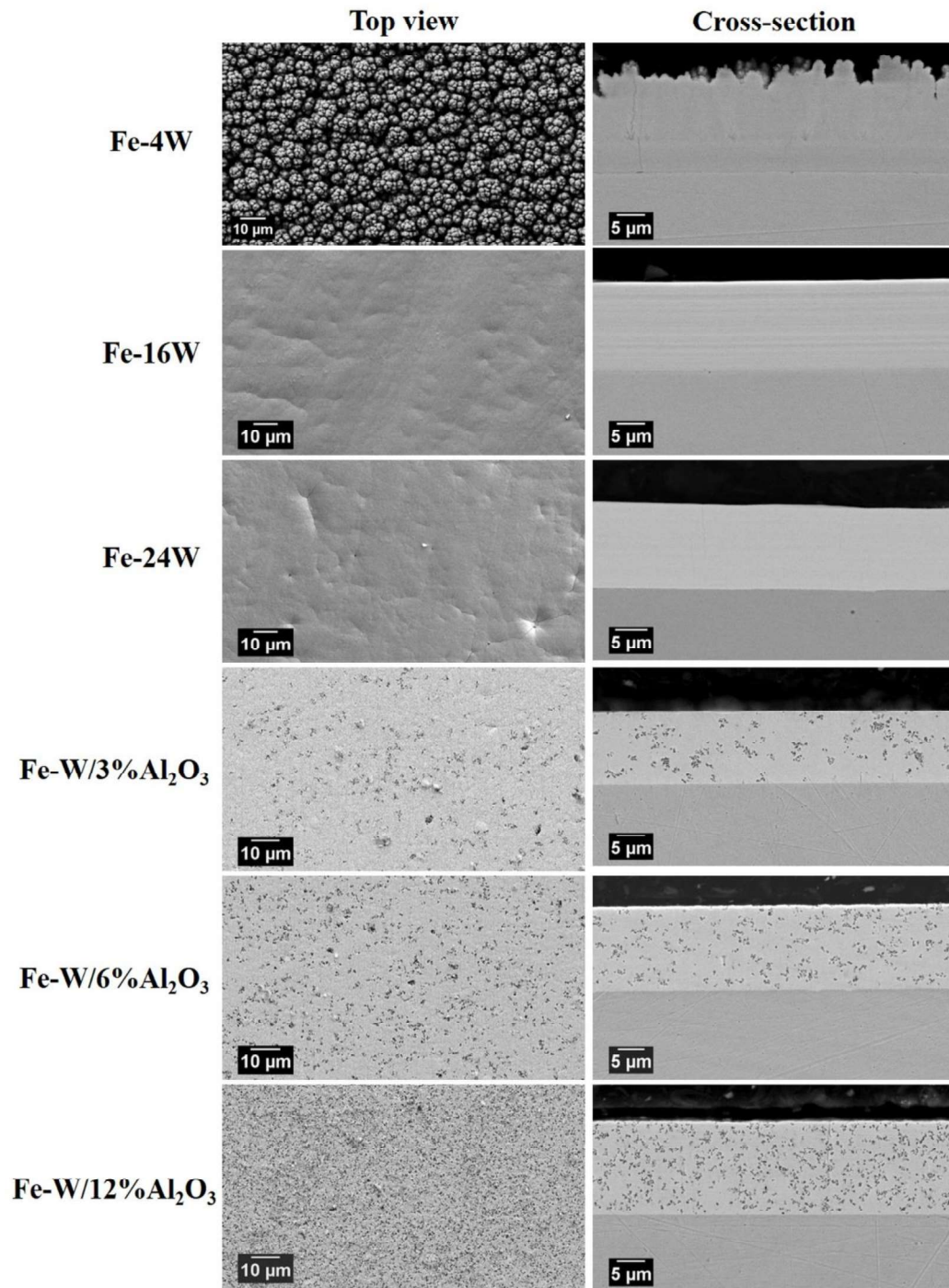


Figure 9. Surface morphology and cross-section of the electrodeposited Fe-W and Fe-W/Al<sub>2</sub>O<sub>3</sub> coatings.



## 4 Characterization techniques

Different techniques were employed to study the microstructure and the properties of the electrodeposited Fe-W and Fe-W/Al<sub>2</sub>O<sub>3</sub> coatings. The methodology followed to characterize the Fe-W alloys studied in this thesis work can be schematized as shown in Fig. 10. The different techniques used to characterize the Fe-W alloys are presented in this chapter.

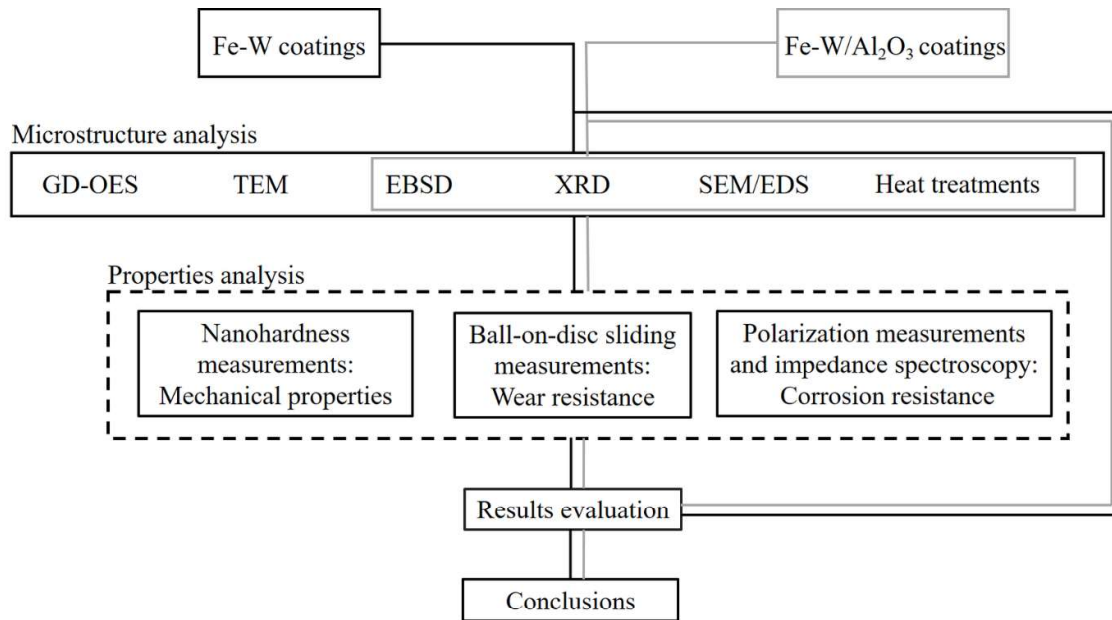


Figure 10. Schematic representation of the research method applied to study the Fe-W and Fe-W/Al<sub>2</sub>O<sub>3</sub> coatings.

### 4.1 Imaging techniques

#### 4.1.1 Optical microscopy

Light Optical Microscopy (LOM) is a primary technique used for sample imaging. In this work, LOM analyses were performed to measure the surface roughness and the wear track profiles for the Fe-W and Fe-W/Al<sub>2</sub>O<sub>3</sub> samples (Paper V, VI and VII). In particular, a LEICA DCM 3D optical microscope was used to measure the wear track profiles, whereas a WYKO Rough Surface Tester Light Interferometer was used to measure the changes in surface roughness caused by the heat treatments.

#### 4.1.2 Scanning electron microscopy (SEM)

Scanning electron microscopy is one of the most versatile technique to analyse microstructural characteristics and to obtain chemical information of solid materials. In SEMs, electrons are used as imaging source. They are generated in an electron gun and are accelerated through apertures at a potential of several keV. The electron beam is then focused onto the surface of the sample by means of electric and magnetic lenses. The interactions between the electrons and the atoms in the sample result in emission of various signals. The emitted radiations are generated from the interactions at different depths of the so-called three-dimensional interaction

volume [85]. In Fig. 11 is shown a schematic representation of the interaction volume and of the different signals generated. The size of the interaction volume is in the range of few micrometres and it varies depending on several factors, e.g. the atomic number of the analysed material, the accelerating voltage of the electron beam and its angle of incidence

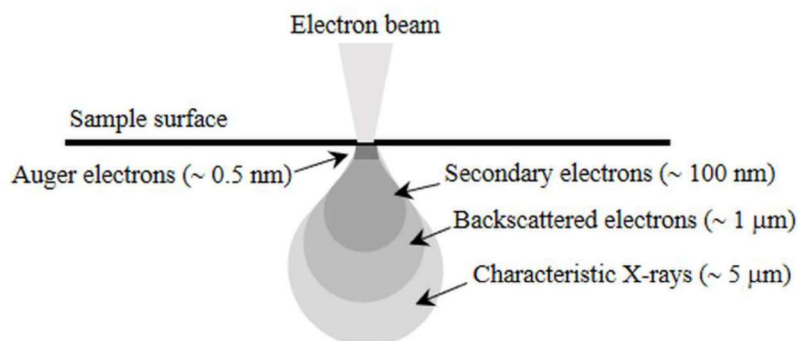


*Figure 11. Schematic representation of the electron beam-sample interaction volume and the signals generated in the SEM.*

The generated signals shown in Fig. 11 can be detected and used for imaging and analysis. Secondary electrons (SE) and backscattered electrons (BSE) are the signals commonly used for imaging. SE are the electrons emitted from the sample by the inelastic scattering of the electron beam. SE have low kinetic energy ( $\leq 50$  eV), therefore only the SEs from depths of  $\sim 100$  nm are able to escape the sample and can be used for imaging surface topography. BSE are generated from elastic scattering of the electron beam. They are highly energetic electrons and thus they can escape from a depth of around  $1 \mu\text{m}$ . The elastic scattering is strongly dependent on the atomic number of the element present in the specimen. Thus, BSE can be used to obtain chemical contrast imaging: atoms of heavy elements backscatter more electrons and will appear brighter. The excess energy related to the interaction between the electrons and the atom of the sample is emitted in form of X-rays. The inelastic scattering of the electron beam with the specimen causes the emission of inner shell electrons, leaving the specimen's atoms ionized. The atom returns to its fundamental state by filling the inner vacant electron site with an outer shell electron. The excess energy released during the process in the form of X-ray photons is characteristic of the electronic structure of the analysed material. Thus, energy dispersive spectroscopy (EDS) analysis uses such X-ray signals for chemical composition analysis. The interaction volume of X-rays is generally in the range of  $\sim 5 \mu\text{m}$ .

A significant part of the SEM characterizations included in this thesis was performed using a Leo 1550 Gemini Scanning Electron Microscope with field emission gun. In addition to SEM imaging, Energy Dispersive X-ray spectroscopy (EDS) and Electron Backscatter Diffraction (EBSD) techniques were applied to characterize the Fe-W alloys.

#### **4.1.3 Electron back scatter diffraction (EBSD)**

EBSD is a characterization technique available in SEMs which provides microstructure and texture information of crystalline materials. The EBSD technique makes use of diffraction patterns generated from the interaction of the focused electron beam with a crystalline

specimen. To obtain such information, the examined specimen requires to be highly polished and to be tilted by  $70^\circ$  relative to the horizon, as shown in Fig. 12a. The scattering events caused by the electrons-sample interaction generate electrons travelling in all conceivable directions (i.e. diffuse scattering). The diffracted electrons that satisfy the Bragg's diffraction condition (see chapter 4.2.1) generate diffraction cones, two parallel cones per each atomic plane, which are detected from the phosphor screen of the EBSD detector (see Fig. 12b). The arcs of the diffraction cones which appear in the phosphor screen produce a pattern of lines, as shown schematically in Fig. 12b. Such diffraction pattern is referred to as Kikuchi pattern and it consists of pairs of parallel lines, i.e. Kikuchi lines, (see Fig. 12c) [86]. The Kikuchi diffraction pattern is characteristic of the crystal structure of the analysed material. For example, the Kikuchi bands (i.e. pairs of Kikuchi lines) identify crystallographic planes, whereas the intersections of the Kikuchi bands correspond to crystallographic directions in the crystal. A camera records the obtained Kikuchi pattern and an automated computer system analyses the Kikuchi bands and their intersections to extract crystallographic information. In fact, by providing a priori information regarding the crystal phases present in the specimen, the computer software indexes the acquired EBSD patterns by comparison with crystallographic data of the expected phases. In the case of poor EBSD pattern quality, e.g. due to overlapping patterns from adjacent grains, or due to the presence of an undefined phase or amorphous phase, the software is not able to index the EBSD pattern which is recorded as a "zero-solution". EBSD analysis can be performed at a specific location (i.e. spot analysis) or by scanning the electron beam with a chosen step size over a defined area of the specimen.

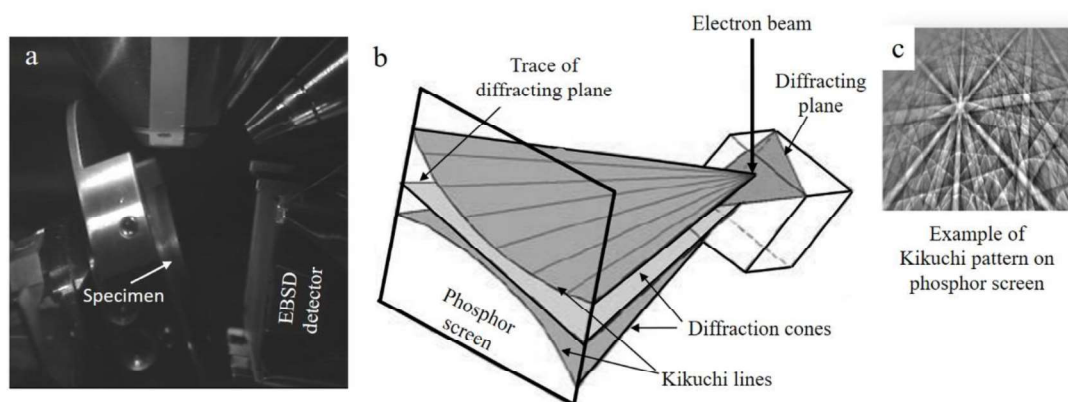


Figure 12. EBSD setup in SEM (a) and schematic representation of the EBSD pattern generated from the interaction of the electron beam with a crystalline specimen, and representative example of a Kikuchi pattern (c). The image in (b) is adapted by permission from Springer Nature: Springer, *Electron Backscatter Diffraction in Materials Science* by Schwartz, A. J., Kumar, M., Adams, B. L., & Field, D. P. (2009) [87].

In this thesis, EBSD technique was used to perform phase discrimination and describe the microstructure (phase distribution and grain sizes) of annealed Fe-W samples (Paper III, IV and V), as well as to perform grain orientation determination (Paper VI). The EBSD data was obtained using an HKL Nordlys EBSD detector (Oxford Instruments). Phase maps and local misorientation maps were created using the HKL Channel 5 software (Oxford Instruments). The EBSD maps were acquired from the cross-section of the Fe-W and Fe-W/ $\text{Al}_2\text{O}_3$  samples, applying an accelerating voltage of 20 kV and a step size of 20 nm. When multiple maps were acquired, those were afterwards stitched together using the Map Stitcher software (Oxford

Instruments). Post processing of the EBSD maps was done with the HKL Channel 5 software and included wild spikes removal and minor noise reduction (4 nearest neighbours required). In the EBSD maps, high angle grain boundaries are shown as black lines and are defined by a misorientation larger than  $10^\circ$ .

#### **4.1.4 Transmission electron microscopy (TEM)**

Transmission electron microscopy allows to perform detailed microstructural analysis with high spatial resolution. When working with a TEM, the applied accelerating voltage is much higher than in SEMs, i.e. generally between 100 kV and 300 kV. In TEMs, the high-energy electron beam passes through a thin sample (i.e. the sample is required to be thin enough to be transparent to the electron beam). Part of the electrons pass through the sample unaffected; the remaining part of the electrons are diffracted, i.e. their trajectory changes due to the interaction with the atoms in the specimen. By adjusting the objective aperture, either the diffracted or the unaffected electrons can be used for imaging. A bright field image is obtained by selecting the direct beam, whereas a dark field image is obtained by selecting the diffracted beam. In TEMs, it is also possible to alternate between imaging and diffraction mode by adjusting the strength of the intermediate lens/diffraction lens. The diffraction mode allows to obtain and analyse diffraction patterns, which contain information on the crystal structure of the analysed sample. A schematic representation of the diffraction pattern obtained when analysing a single crystal, a polycrystalline and an amorphous material is shown in Fig. 13.

In this thesis work, TEM imaging and diffraction analysis of the as-deposited Fe-24W sample was performed using a Zeiss EM 912 Omega transmission electron microscope (Paper II). In-situ TEM analyses were conducted in a JEOL JEM 2200FS, while EDS analyses were performed in a TEM of type FEI Titan 80-300 (Paper IV). The specimens used for the investigations were a substrate-free sheet with a thickness of around 15  $\mu\text{m}$ . Discs with a diameter of 3 mm were punched from the sheet and then thinned by ion milling with a Gatan precision ion polishing system. To obtain electron-transparent specimens, the discs were ion milled with an angle of incidence of  $6^\circ$  until a small hole was obtained in the middle of the disc. The area around the hole was thinned further with an angle of incidence of  $4^\circ$ .

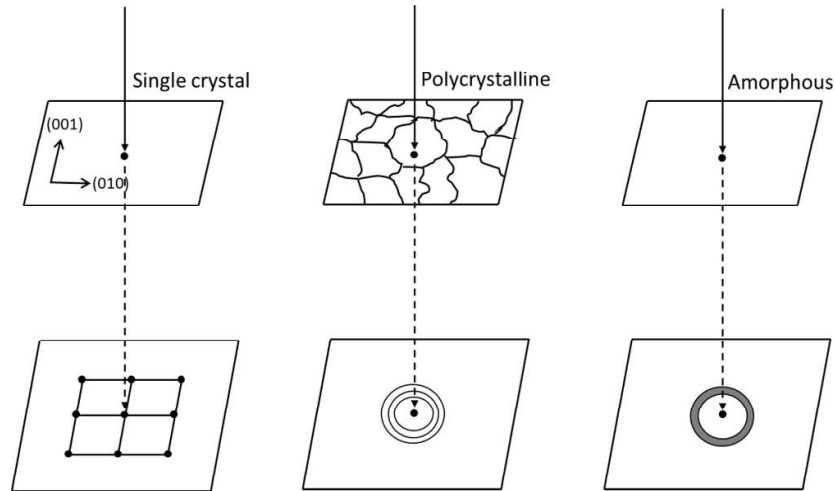


Figure 13. Schematic representation of different diffraction pattern obtained from a single crystal, polycrystalline and amorphous material, adapted from [88].

## 4.2 Non-imaging techniques

### 4.2.1 X-ray diffraction (XRD)

X-ray diffraction is a commonly used technique for phase identification analysis. Its working principle is based on X-ray diffraction as described by Bragg's law:

$$n\lambda = 2d \sin \theta$$

Where  $n$  stands for the diffraction order,  $\lambda$  for the wavelength of the X-ray beam,  $d$  for the interplanar distance, and  $\theta$  for the diffraction angle. Phase identification is performed by converting the angles where constructive interference of X-rays occurs into interplanar distances. The sets of diffraction planes are then compared with diffraction planes from a standard database.

In this thesis work, XRD analysis were performed with a Rigaku MiniFlex II diffractometer with Cu  $K\alpha$  radiation,  $\lambda=1.54183 \text{ \AA}$ , (Paper II, III and VI) and a Bruker AXS D8 advance diffractometer with Cr  $K\alpha$  radiation,  $\lambda =2.28970 \text{ \AA}$ , (Paper IV, V and VII). With the Bruker AXS D8 advance diffractometer, XRD spectra were acquired both with Bragg-Brentano  $\theta/\theta$  and grazing incidence (GIXRD) geometries. A schematic representation of both geometries is provided in Fig. 14. For the GIXRD configuration, the angle of incidence  $\alpha$  was set to  $3^\circ$ .

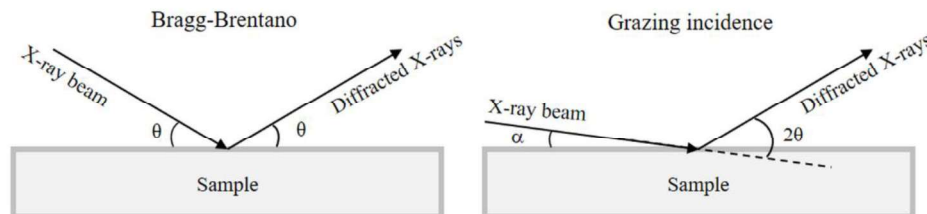


Figure 14. Schematic representation of Bragg-Brentano  $\theta/\theta$  and grazing incidence geometries.

#### **4.2.2 Glow discharge optical emission spectroscopy (GD-OES)**

Glow Discharge Optical Emission Spectroscopy (GD-OES) is a destructive spectroscopic technique for qualitative and quantitative chemical analysis. This technique is commonly employed to obtain compositional depth profiles (CPD) of relatively thick layers (i.e. several tens of micrometers). One of the main advantages of the technique is its high sensitivity for both heavy and light elements (e.g. O, C and H). GD-OES measurements are performed by applying a voltage between an electrode and the sample to be analysed (the cathode) which are placed in a chamber filled with an inert gas such as Ar. In the GD-OES chamber a glow discharge plasma is generated with the sample acting as a cathode. The cations present in the plasma are accelerated toward the sample surface and they progressively remove atoms from the sample (sputtering process). The ejected atoms interact with the plasma and emit photons with characteristic wavelengths. The photons are collected and analysed, which results in quantitative chemical information of the analysed sample.

The instrument used in this thesis work (Paper II) was a GDA750HR (Spectrumba) with 2.5 mm source in DC mode. The discharge was operated in a high-purity Ar atmosphere and constant current (10 mA)/constant voltage (700 V) control mode.

#### **4.2.3 Heat treatments**

Heat treatments in vacuum and in Ar atmosphere were performed in order to study the thermal stability and the occurring microstructural transformations in the Fe-W and Fe-W/Al<sub>2</sub>O<sub>3</sub> coatings. Vacuum heat treatments (Paper II, III and IV) were performed to minimize the influence of annealing atmosphere (e.g. oxygen impurities) on the microstructural transformation of the annealed samples. Heat treatments of Fe-W and Fe-W/Al<sub>2</sub>O<sub>3</sub> coatings were also performed in Ar atmosphere (Paper V, VI and VII) considering that Ar annealing is more commonly employed in industry.

The vacuum heat treatments were performed in a controlled vacuum chamber ( $1 \times 10^{-8}$  Pa). The chamber was heated at 200, 400, 600 and 800 °C. Once the chamber reached the selected temperature, the samples (1x1 cm) were inserted and kept for one hour. The samples were cooled down to room temperature inside the furnace. For the heat treatments under Ar atmosphere, the Fe-W and Fe-W/Al<sub>2</sub>O<sub>3</sub> samples (2 x 2 cm) were inserted in the furnace of a NETZSCH 402 C dilatometer (Burlington, MA, USA). A heating rate of 20 °C/min was applied and the samples were kept for one hour at 200, 400, 600 and 800 °C. Afterwards, the samples were cooled down to room temperature inside the furnace.

#### **4.2.4 Differential scanning calorimetry (DSC)**

Differential scanning calorimetry is a technique used to measure the heat flow difference between the analysed sample and a reference. A DSC curve is then obtained by plotting the difference in heat flow between the sample and the reference as a function of temperature. The measured event can be either endothermic or exothermic, i.e. the heat is either absorbed or released by the sample because of the occurring microstructural transformation. DSC measurements are employed to determine the temperature associated to transformation events such as crystallization, phase transformation, grain growth and even magnetic transition (e.g. the Curie point).

DSC measurements were performed using a thermal analyser STA 449 F1 Jupiter from Netzsch (Paper IV). The Fe-24W sample was loaded in a PtRh/Al<sub>2</sub>O<sub>3</sub> crucibles and heated up to 800 °C with a heating rate of 10 °C/min under Ar atmosphere. To highlight the irreversible transformations occurring upon annealing, i.e. crystallization of the amorphous structure, two successive heating scans were performed for the same sample. As shown in the schematic plot in Fig. 15, by subtracting the second scan, it is possible to separate the reversible transformations (e.g. ferromagnetic transition) from the irreversible transformations.

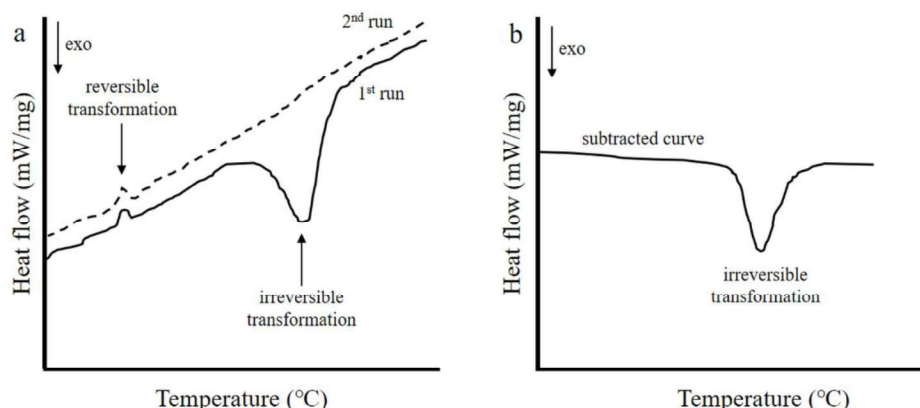


Figure 15. Schematic plot of a DSC curve from a first and second heating run (a), and DSC curve after subtraction of the second heating run (b). Plot inspired by [89].

#### 4.2.5 Nanohardness measurements

Nanoindentation is a common technique used to study the mechanical behaviour of materials at a small scale. In general, indentation techniques are applied to measure the resistance of the material to the local plastic deformation that is induced by the indenter. During a nanoindentation test, the sample is loaded by the indenter and the variation in time of the penetration depth with respect to the applied load is recorded, as shown in Fig. 16. From the final penetration depth ( $h_f$ ) and the elastic unloading stiffness ( $S$ ) obtained from the load-displacement curve (see Fig. 16), the hardness ( $H$ ) and the elastic modulus ( $E$ ) of the material can be determined according to the Oliver-Phar method [90].

In this thesis work, nanohardness measurements were performed on the cross-sections of the as-deposited and annealed Fe-W and Fe-W/Al<sub>2</sub>O<sub>3</sub> coatings (Paper III, VI and VII) using a NHT2 Nanoindentation Tester from Anton-Paar. The hardness tester was equipped with a Berkovich pyramidal-shaped diamond tip, the measurements were done underload-control mode with a loading time of 30 seconds, followed by a load holding segment of 10 seconds, and by an unloading segment of 30 seconds. A load of 10 mN was applied for the Fe-W coatings, whereas 25 and 50 mN load was applied for the Fe-W/Al<sub>2</sub>O<sub>3</sub> coatings. The higher load applied for the Fe-W/Al<sub>2</sub>O<sub>3</sub> coatings was selected in order to include both alumina particles and Fe-W matrix in the indentation imprints (as shown in the SEM image in Fig. 16).

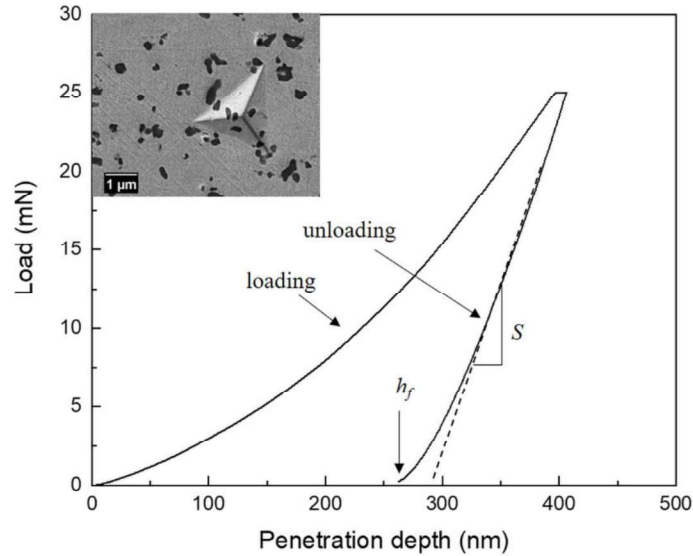


Figure 16. Load versus penetration depth curve measured for as-deposited Fe-W/Al<sub>2</sub>O<sub>3</sub>. The insert shows a representative SEM image of an indent imprint on the cross-section of the composite coating.

#### 4.2.6 Ball-on-disc measurements

In a tribometer tester, a static counter material (i.e. the ball) is mounted on a stiff cantilever and placed in contact with the sample to be analysed (i.e. the disc). The sliding movement is provided by an electric motor connected to the sample holder, and the load is applied by adding a weight on top of the stiff cantilever. The tribometer records in time the friction coefficient between the counter material and the sample by measuring the deflection of the cantilever. The measured deflection is proportional to the frictional force.

The ball-on-disc tests were performed using a CSM Instruments sliding tester, model THT, in dry conditions and with an alumina ball of 6 mm diameter counter-body. A load of 2 N was applied with a rotation speed of 4 cm·s<sup>-1</sup> for 500 m and with a fixed rotation diameter of 2.5 mm (Paper V and VII) and 6 mm (Paper VI). Three wear tests per specimen were performed. The applied wear parameters were selected in consideration of previously published work on the wear resistance of electrodeposited Fe-group metal coatings and did not intend to simulate the condition of a specific wear-critical application. After each wear test, the wear rate of the coatings was calculated according to the following equation:

$$K = \frac{Al}{FD}$$

where  $A$  is the cross-section area of wear track (mm<sup>2</sup>),  $l$  is the length of the wear track (mm),  $F$  is the load (N) and  $D$  is the sliding distance (m).

#### 4.2.7 Potentiodynamic measurements and electrochemical impedance spectroscopy

Potentiodynamic measurements are electrochemical tests commonly used to evaluate the corrosion behaviour of a material in a specific aqueous environment. The measurements are performed with a three-electrode set-up consisting of the material to be tested (i.e. the working electrode), a counter electrode and a reference electrode. The electrodes are placed in a solution

simulating a corrosive environment for the application of the studied material. The measurement is conducted by varying the voltage applied between the working and reference electrode, while measuring over time the circulating current. In Paper VI, potentiodynamic measurements were performed in a 0.1 M NaCl solution, varying the potential between -1 and 1 Volt with a sweep rate of 1mV/s.

Electrochemical impedance spectroscopy (EIS) tests are applied to study the kinetics of the corrosion of metals and alloys. The working principle is based on applying sinusoidal potential perturbation at different frequencies, while measuring the response of the electrode (i.e. the sample) to the applied perturbations. The EIS experimental data are afterwards fitted to an equivalent electrical circuit. The element composing the electrical circuits (e.g. resistance and capacitance) are then related to physical processes in the system (e.g. double layer capacitance, charge transfer resistance). In Paper VI, EIS measurements were performed in a 0.1 M NaCl solution by applying a sinusoidal voltage with 5 mV amplitude in the frequency range of 10 kHz to 0.01 Hz. The fitting of the EIS data was done using a Z-view software.



## 5 Summary of results and discussions

This chapter provides a summary of the results which are discussed in the seven papers appended to this thesis. The results are presented following the order of the research approach steps described in chapter 1.3. Hence, first, the influence of the composition on the structure and thermal stability of various Fe-W coatings is discussed. The observed microstructural transformations are linked to mechanical properties (i.e. hardness and reduced elastic modulus) and to the wear resistance of the Fe-W coatings. Finally, the influence of co-deposited alumina particles on the mechanical properties, corrosion and wear resistance is discussed.

### 5.1 Interdependences between the composition, the structure and the thermal stability of Fe-W coatings

As previously mentioned, increasing the amount of co-deposited W is often associated with a grain size reduction and with a transition from a nanocrystalline to amorphous structure. This transition in the structure is also observed from the XRD results acquired from the as-deposited Fe-W coatings, see Fig. 17. A nanocrystalline structure is found for the Fe-4W sample, a mixed nanocrystalline-amorphous structure for the Fe-16W sample, and a homogeneous amorphous structure for the Fe-24W sample. For the Fe-16W sample, the presence of a small crystalline peak in the XRD profile indicates a certain degree of crystallinity of the sample's structure. The amorphous structure of the Fe-24W sample is indicated by the broad halo without well-defined peaks in the XRD profile of the sample. The TEM image in Fig. 17b, acquired from the same sample shows a “maze-like” contrast and a selected area diffraction pattern (SAD) (shown as inset) with a single, broad ring which confirms the amorphous nature of the Fe-24W sample [91].

To study the thermal stability and the microstructural transformations occurring upon annealing of the Fe-W coatings, heat treatments were performed between 200 °C and 800 °C both in vacuum and in Ar atmosphere for 1 hour. The results are presented in the following paragraphs.

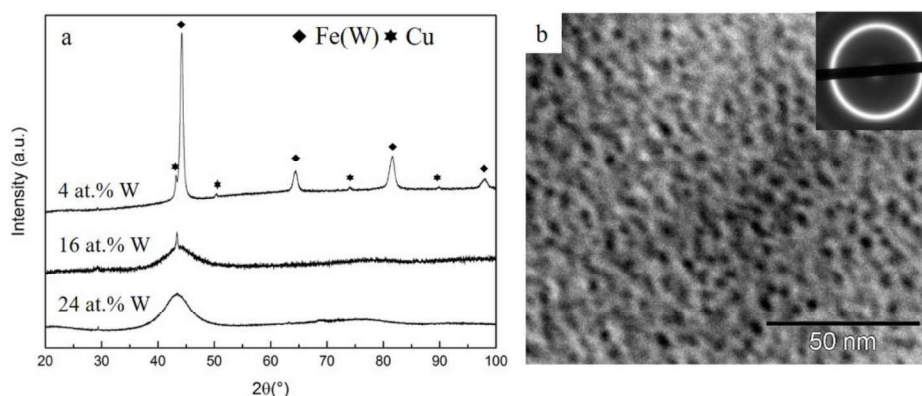


Figure 17. X-ray diffraction profiles of the as-deposited Fe-W samples (a), and TEM image of the Fe-24W sample including an inset of a SAD pattern acquired from the sample (b).

## Vacuum heat treatments of Fe-W coatings

The microstructural transformations occurring in the Fe-W samples at each annealing temperature are shown in Fig. 18. The results reveal that the thermal stability of Fe-W alloys increases with increasing the amount of the co-deposited W. In general, it has been observed that the addition of a high melting point element (such as W) slows down the elemental diffusion in the samples, thus resulting in an increased thermal stability [92]. Minor changes are observed in the structure of the Fe-4W sample: the crystalline peak of the Fe(W) solid solution is shifted toward higher diffraction angles (approaching the diffraction angle of  $\alpha$ -Fe). Also, the crystalline peak appears narrower with increasing the annealing temperature, which indicates the occurrence of grain growth. The Fe-16W sample is fully crystallized after annealing at 400 °C, whereas the Fe-24W sample retains the amorphous structure up to 600 °C where a partially crystallized structure is observed due to the formation of  $\alpha$ -Fe crystalline phase. The Fe-24W sample is still not fully crystalline after annealing at 800 °C (~30% of retained amorphous phase, as calculated from XRD results). This is also visible by the retained amorphous halo which is still observed in the XRD profile after annealing at 800 °C for 6 and 12 h, respectively (see Fig. 3 in Paper III). These results highlight the outstanding thermal stability of the Fe-24W sample. As shown in Fig. 18, the crystallization of the Fe-W coatings upon annealing led to the formation of the following phases:  $\alpha$ -Fe, Fe<sub>2</sub>W, Fe<sub>3</sub>W<sub>3</sub>C, Fe<sub>6</sub>W<sub>6</sub>C, and FeWO<sub>4</sub>. The formation of  $\alpha$ -Fe and of the intermetallic Fe<sub>2</sub>W is expected according to the binary Fe-W phase diagram [93,94]. The formation of the carbide and the oxide phases upon annealing can be related to the presence of O and C as co-deposited impurities, as observed from GD-OES analysis (see Fig. 4 in Paper II).

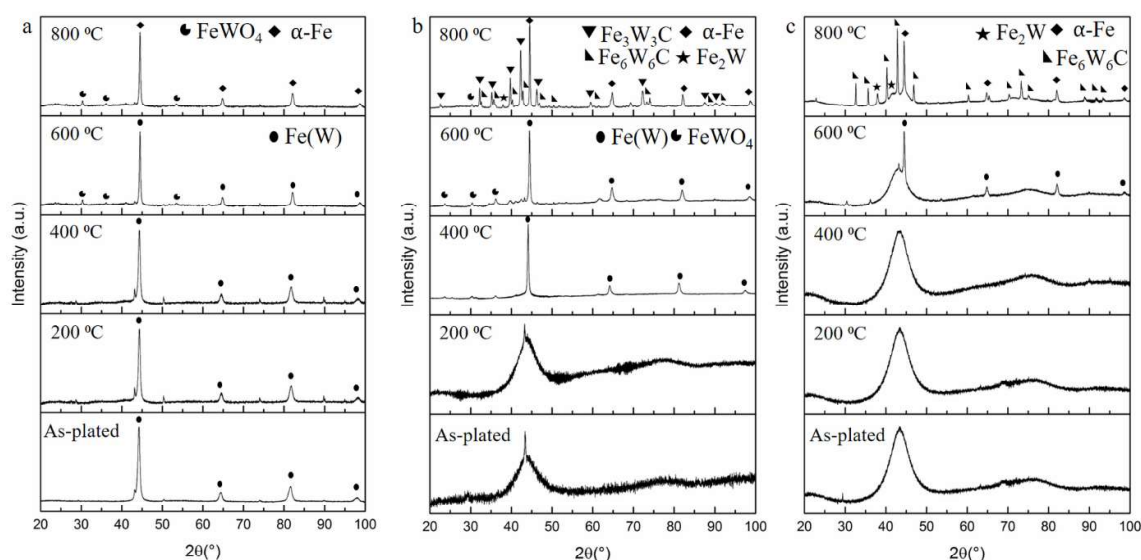


Figure 18. X-ray diffraction profiles of the Fe-4W (a), Fe-16W (b), and Fe-24W sample (c) annealed at different temperatures.

To study the distribution of the observed crystalline phases, EBSD analyses were performed on selected areas of the cross-section of the samples annealed at 800 °C. Figure 19 shows the back scattered electron images of cross-sections together with the EBSD phase maps. The boxes in

the SEM images marked with red dashed lines define the areas where the EBSD phase maps were acquired. As shown in Fig. 19a, the structure of annealed Fe-4W sample is characterized by large  $\alpha$ -Fe grains (a few micrometres in size) and  $\text{FeWO}_4$  grains which are distributed along the sample thickness. In the phase map of the Fe-16W sample, three crystalline phases are identified:  $\alpha$ -Fe,  $\text{Fe}_6\text{W}_6\text{C}$  and  $\text{FeWO}_4$ . As compared to the Fe-4W sample, the grain size of the  $\alpha$ -Fe phase is smaller in the Fe-16W sample ( $\sim 200$  nm average grain size, see Fig. 6 in Paper III), and both the carbide and the oxide phases are distributed across the entire coating thickness. The fraction of indexed  $\text{Fe}_2\text{W}$  and  $\text{Fe}_3\text{W}_3\text{C}$  phases was very low, i.e. below 1%, and for this reason both phases were excluded from the analysis. Similar  $\alpha$ -Fe grain sizes are observed for the Fe-24W sample annealed at  $800^\circ\text{C}$  ( $\sim 150$  nm grain size). However, the acquired phase map is characterized with a large fraction of zero solutions, which is shown as white pixels/areas in the phase map. Such high fraction can be related to the nanocrystalline/amorphous nature of the sample which is preserved after the heat treatment and thus not possible to be indexed by EBSD technique.

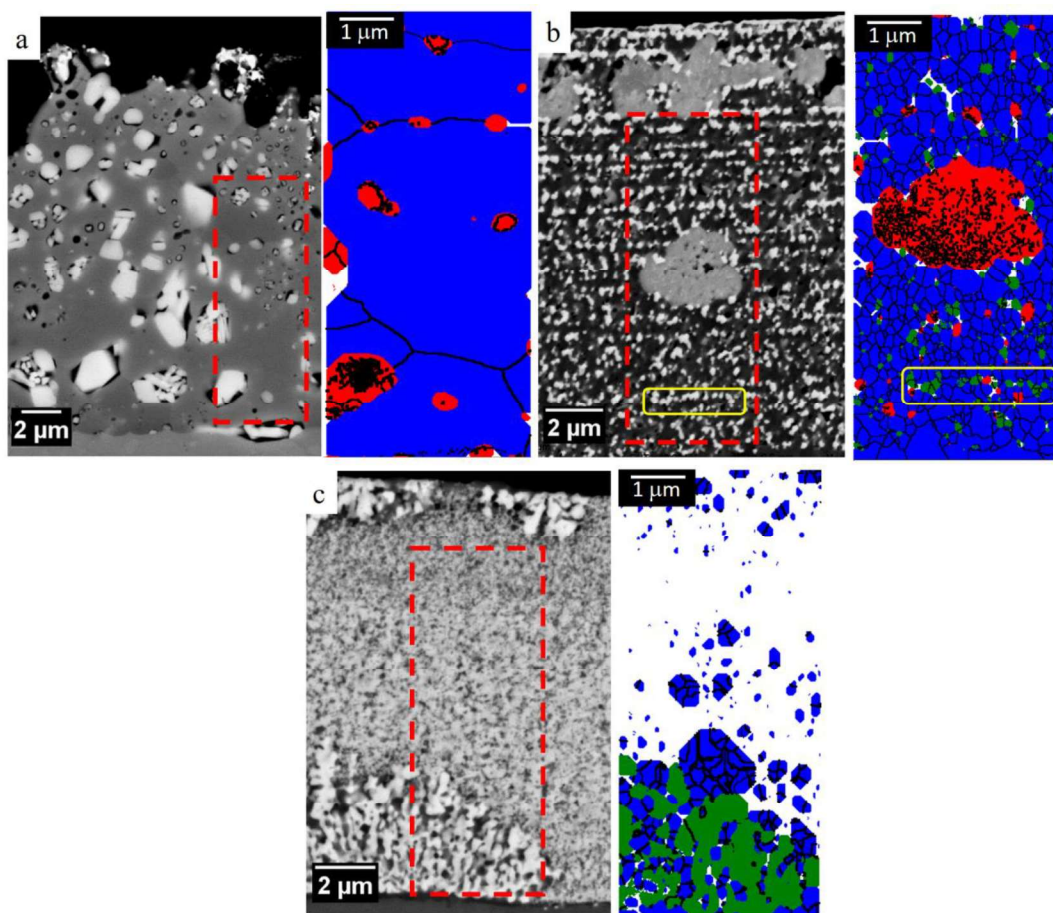
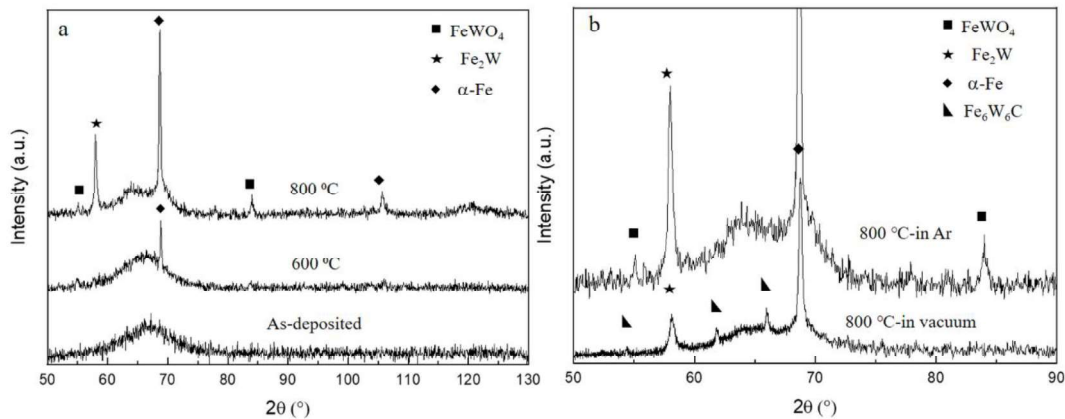


Figure 19. BSE image and phase map of the cross-section of the Fe-4W (a), Fe-16W (b), and Fe-24W sample (c) annealed at  $800^\circ\text{C}$  for 1 hour. The EBSD phase maps are acquired from the red dashed boxes highlighted in each sample cross-section. The following color code is used in the figure: blue grains belong to  $\alpha$ -Fe phase, the red grains to the  $\text{FeWO}_4$  phase, and the green grains to the  $\text{Fe}_6\text{W}_6\text{C}$  phase.

### Argon heat treatments of Fe-24W coatings

For the Fe-24W coatings, additional heat treatments were performed between 200 °C and 800 °C in Ar atmosphere. Up to 600 °C, the microstructural transformations are the same as observed after heat treatment in vacuum: a partially crystallized structure is formed with  $\alpha$ -Fe as crystalline phase, see Fig. 20a. However, annealing at 800 °C in a slightly oxidizing atmosphere (such as Ar atmosphere) favours the crystallization of the  $\text{FeWO}_4$  instead of the  $\text{Fe}_6\text{W}_6\text{C}$  phase formed when annealing in vacuum. This finding is strengthened by the XRD diffraction profiles in Fig. 20b showing the same Fe-24W sample after annealing at 800 °C in vacuum and in Ar, respectively.



*Figure 20. X-ray diffraction profiles showing the different phase transformation occurring for the Fe-24W sample annealed in Ar (a), comparison of the X-ray diffraction profiles when annealing Fe-24W sample at 800 °C in Ar and in vacuum atmosphere.*

The observed crystallographic transformations of the Fe-W coatings are expected to influence the mechanical and wear properties of the coatings as described in the following paragraphs. In particular, the mechanical properties (i.e. hardness and Young's modulus) described in chapter 5.2 were measured after vacuum heat treatments. The wear resistance of Fe-24W and Fe-W/12Al<sub>2</sub>O<sub>3</sub> coatings, described in chapter 5.3 and 5.5, was studied after heat treatments in Ar atmosphere.

## 5.2 Heat treatment effects on the hardness and elastic modulus of Fe-W coatings

Several studies have shown that the microstructural transformation occurring upon heat treatment of binary and ternary W-containing electrodeposits (e.g. Ni-W, or Ni-Fe-W) can improve the mechanical properties of the alloys [65,95,96]. Therefore, the hardness and the reduced elastic modulus of the as-deposited and annealed Fe-W coatings were measured by nanoindentation and the results are shown in Fig. 21. In the as-deposited condition, the Fe-24W coating is characterized with the highest hardness and reduced elastic modulus, owing to the high amount of co-deposited W and to the W-induced amorphization observed in the sample. Furthermore, an increase in the hardness is obtained upon annealing at 400 °C and 600 °C, where the maximum hardness and modulus are observed, i.e. 16.5 and 219 GPa, respectively. As shown in Fig. 18c, XRD analysis on the Fe-24W sample annealed at 400 °C did not reveal any crystallization that could be related to the observed hardness increase. However, in-situ TEM annealing of the Fe-24W sample (Paper IV) revealed the formation of first crystallites after 30 minutes annealing at 400 °C, see Fig. 22. The crystallization is more evident when annealing between 500 and 600 °C, with the formation of ~40 nm nanocrystals dispersed in the amorphous matrix (Fig. 22). Hence, the increase in mechanical properties of the annealed Fe-24W coating is related to the formation of crystallites, starting from 400°C, which results in the formation of a mixed nanocrystalline-amorphous structure. In fact, previous studies on the crystallization of Fe and Zr-based bulk metallic glasses have shown that the formation of nanocrystalline grains embedded in an amorphous structure can cause a significant increase in the hardness and elastic modulus of the material [97,98]. A strengthening effect is also observed upon annealing of Fe-16W sample, but it is less pronounced as compared to the Fe-24W sample. A substantial decrease in the hardness of both Fe-16W and Fe-24W coatings is observed after annealing at 800 °C due to the grain growth of  $\alpha$ -Fe crystalline phase, reaching an average grain size of ~200 nm (see Fig. 6 in Paper III). The same mechanism is observed for the Fe-4W sample. Here, due to the lower co-deposited W, the grain growth is already starting at around 400 °C.

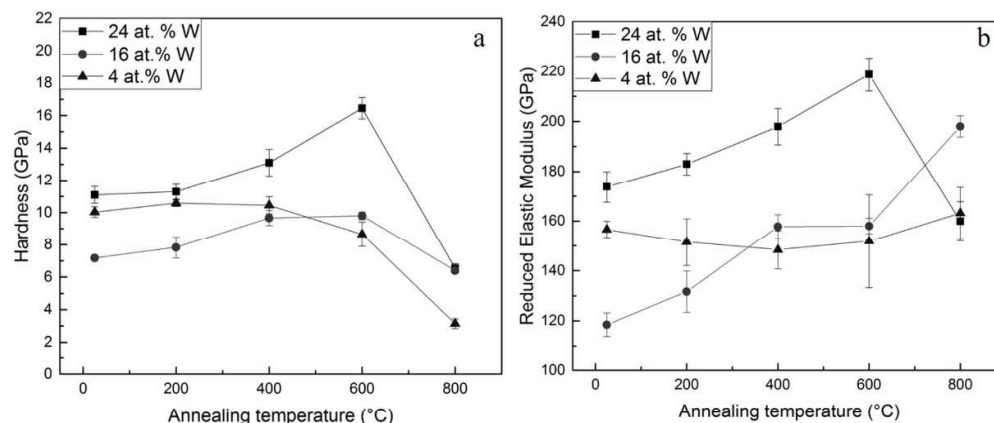


Figure 21. Hardness (a) and reduced elastic modulus (b) of Fe-W coatings plotted as a function of annealing temperatures.

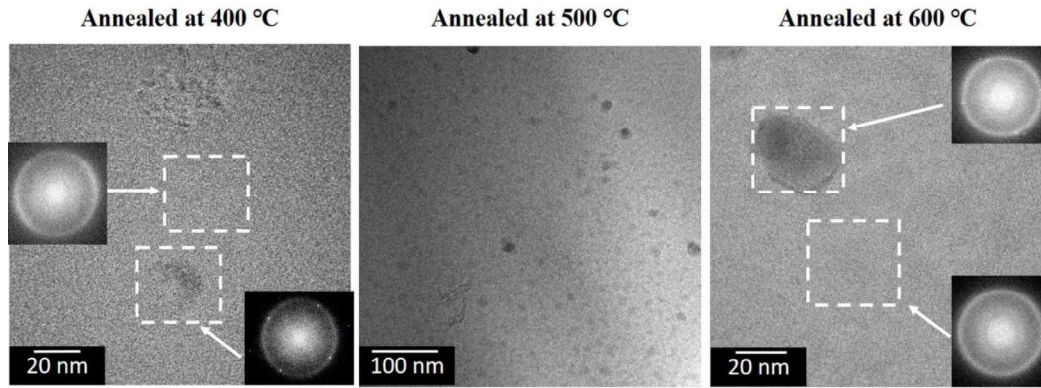


Figure 22. TEM micrographs of Fe-24W sample in-situ annealed at 400, 500 and 600 °C, respectively. The Fast Fourier Transform (FFT) acquired from the white squares in the micrographs are shown as inset.

The variation of the reduced elastic modulus,  $E_r$ , upon annealing of the samples can also be related to the microstructural transformations. The main microstructural transformation occurring during annealing of the Fe-4W sample is the grain growth of nanocrystalline Fe(W) phase. As the elastic modulus is an intrinsic material property and thus not influenced by changes in the grain size, the  $E_r$  remains almost constant with increasing temperature for the Fe-4W sample. For the Fe-16W and Fe-24W samples, the increase in the  $E_r$  observed up to 600 °C can be related to the structural relaxation and annihilation of free volume, which is observed upon annealing of amorphous alloys [99]. The increase of  $E_r$  observed for the Fe-16W sample after annealing at 800 °C is related to the contribution of the  $F_6W_6C$  phase (whose elastic modulus is reported to be ~327 GPa [100]). The same contribution is not expected for the Fe-24W sample because the carbides are located at the substrate-coating interface and at the surface of the coating and are therefore not included in the indents (see Fig. 19).

In summary, the Fe-24W coatings showed the highest hardness both in as-deposited condition and after annealing treatments. Generally, a high hardness can be associated with a high wear resistance. Hence, the as-deposited and annealed Fe-24W coatings were selected as promising candidates for the evaluation of tribological properties.

### 5.3 Wear resistance of as-deposited and annealed Fe-24W coatings

The wear resistance of as-deposited and annealed Fe-24W samples was studied under dry friction conditions using ball-on-disc sliding tests. Figure 23 shows the variation of the coefficient of friction (COF) measured from the as-deposited and annealed samples together with the wear track profiles of the as-deposited sample and the sample annealed at 800 °C, respectively (Fig. 23b and c). Except for the sample annealed at 800 °C, the Fe-24W samples suffered of severe tribo-oxidation which caused the formation of deep cracks along the wear tracks (e.g.  $\sim 15\ \mu\text{m}$  in depth as seen in Fig. 23b) and led to the instability of the measured COF, see Fig. 16a. The occurrence of tribo-oxidation wear mechanism was revealed by SEM and EDS analyses showing traces of adherent oxide along the wear track of the Fe-W sample annealed up to 600 °C (see Fig. 9 in Paper V). The oxidation of the coatings during the sliding test is an intrinsic response of the material to recover from the thermal energy generated during dry friction [101]. The higher wear resistance of the Fe-W sample annealed at 800 °C can be related to the precipitation of the  $\text{Fe}_2\text{W}$  and  $\text{FeWO}_4$  phases upon annealing. As shown from the comparison of the X-ray spectra acquired with Bragg–Brentano and with grazing incidence geometry in Fig. 24, these phases are mostly present in the proximity of the sample surface. Hence, these phases increase the resistance of the sample to tribo-oxidation, leading to a considerable reduction of the wear rate:  $\sim 3 \times 10^{-6}\ \text{mm}^3/\text{Nm}$  as compared to  $\sim 11 \times 10^{-6}\ \text{mm}^3/\text{Nm}$  measured for the as-deposited sample. Furthermore, the wear rate measured for the Fe-24W sample annealed at 800 °C is found to be comparable to the wear rate of hard Cr coatings (see Fig. 8 in Paper V). However, a lower coefficient of friction, i.e.  $\sim 0.6$ , is measured for the hard Cr coating.

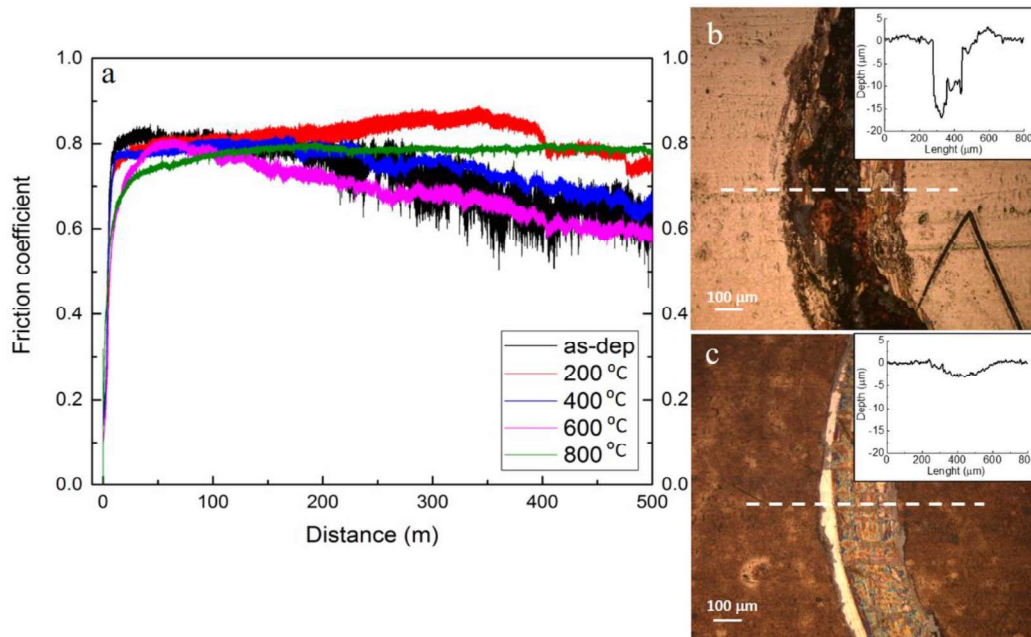
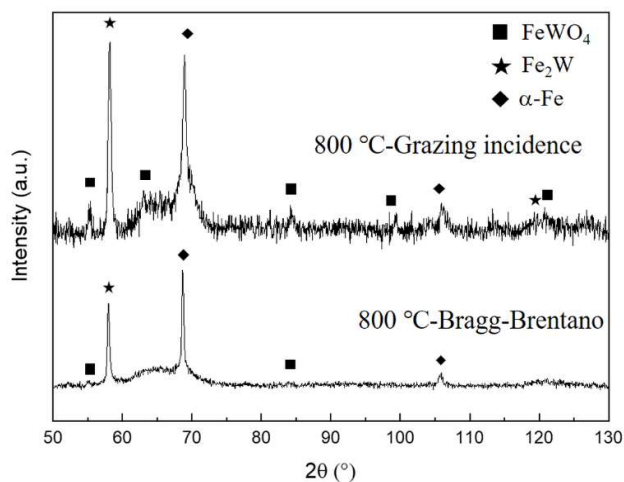


Figure 23. Coefficient of friction (COF) evolution for the as-deposited and annealed Fe-24W coatings (a), together with optical micrographs of the wear track of the as-deposited sample (b), and the sample annealed at 800 °C (c). The surface profiles acquired at the locations of the dashed lines are included as inserts.



*Figure 24. X-ray diffraction profiles of Fe-24W sample annealed at 800 °C acquired with Bragg–Brentano and grazing incidence geometry.*

The deposition of Fe-W/Al<sub>2</sub>O<sub>3</sub> composite coatings was performed aiming to improve the wear resistance (i.e. COF and wear rate) of as-deposited Fe-W alloys. The following paragraph discusses the influence of co-deposited alumina particles on the microstructure and on the wear and corrosion properties of the Fe-W/Al<sub>2</sub>O<sub>3</sub> composite coatings.

## 5.4 Wear and corrosion resistance of Fe-W/Al<sub>2</sub>O<sub>3</sub> composites

As specified in paragraph 3.2, the electrolyte and deposition parameters used to deposit the composites were kept almost identical as for the electrodeposition of Fe-W coatings with high W content. The different amounts of co-deposited Al<sub>2</sub>O<sub>3</sub> were obtained by increasing the concentration of the particles in the bath (i.e. from 25 to 100 g l<sup>-1</sup>). A stirring rate of 200 rpm was applied to facilitate the co-deposition of alumina particles within the Fe-W matrix. For the sake of comparison, and to isolate the effect of the alumina particles on the wear and corrosion resistance, a Fe-W coating free of particles was also deposited using the same deposition conditions.

As shown from the XRD results in Fig. 25, by increasing the amount of co-deposited alumina grain size, a refinement and amorphization of the Fe-W matrix is observed. In fact, already with the co-deposition of 3% of particles the intensity of the Fe(W) crystalline peak is reduced and the broad shoulder starting at ~43 °C can be seen. In the XRD pattern of Fe-W/6%Al<sub>2</sub>O<sub>3</sub> and Fe-W/12%Al<sub>2</sub>O<sub>3</sub> coatings, respectively, only a broad halo is visible. This is attributed to the presence of the alumina particles, as they lead to more active sites for nucleation [102]. An increase in the nucleation mechanism, due to the applied deposition conditions, is considered to determine the grain size refinement in electrodeposited alloys and composites [42].

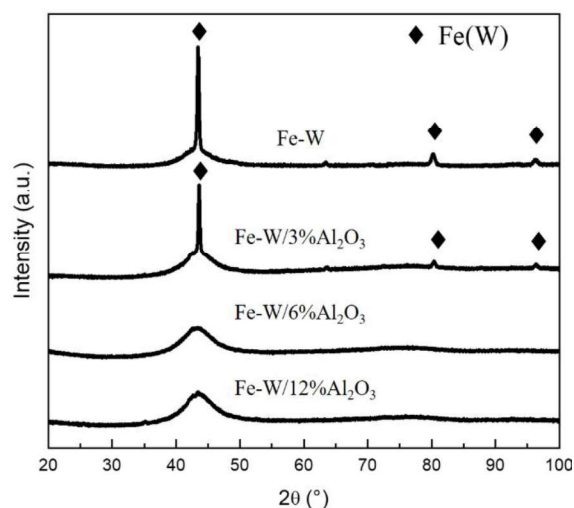


Figure 25. XRD diffraction profiles of Fe-W and Fe-W/Al<sub>2</sub>O<sub>3</sub> composite coatings with different concentration of co-deposited alumina particles.

### Wear resistance of Fe-W/Al<sub>2</sub>O<sub>3</sub> composites

The co-deposition of alumina particles proved to be effective in enhancing the wear resistance of Fe-W alloys, especially for the composite containing the most particles, i.e. 12%. In Fig. 26, the COF and wear rate of the Fe-W and Fe-W/Al<sub>2</sub>O<sub>3</sub> composite samples are presented. The presence of the Al<sub>2</sub>O<sub>3</sub> particles reduces the area of the Fe-W matrix affected by the sliding contact and thus lowers the severity of the tribo-oxidation mechanism. This results in a reduction of both the COF and the wear rate, as shown in Fig. 26.

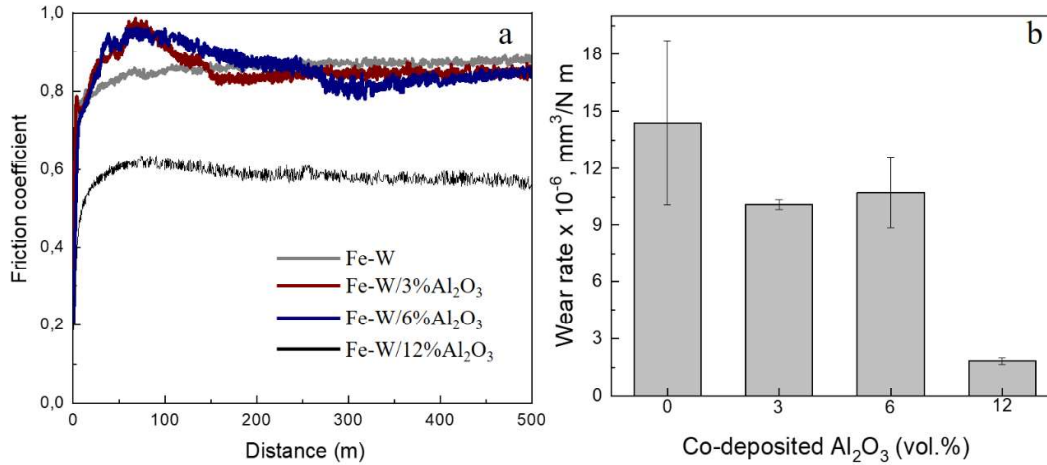


Figure 26. Coefficient of friction evolution (a) and wear rate of Fe-W and Fe-W/Al<sub>2</sub>O<sub>3</sub> composite coatings with different concentrations of co-deposited alumina particles.

#### Corrosion resistance of Fe-W/Al<sub>2</sub>O<sub>3</sub> composites

Selected results from the study of the corrosion resistance of the Fe-W coatings and composites are shown in Fig. 27. Figure 27a illustrates the polarization curves measured in a 0.1 M NaCl solution (the parameters extracted from the curves are included in Table 2), and in Fig. 27b and 27c are presented SEM micrographs of the surface morphology after the corrosion of the Fe-W and Fe-W/12%Al<sub>2</sub>O<sub>3</sub> sample, respectively. The impact of the co-deposited alumina particles on the corrosion resistance appears to be rather limited. The polarization curves of the different sample are very similar (see Fig 27a) and are characterized by the anodic metal dissolution without the presence of a passive state. EDS analysis performed after corrosion tests highlighted an oxygen and tungsten enrichment at the sample surface, up to 50 and 28 at.%, respectively. These results indicate that the corrosion occurs through the dissolution of the Fe, and the formation of iron and iron-tungsten oxides, which is in accordance with previous studies on the corrosion behaviour of electrodeposited Fe-W alloys [103]. Also, the formation of cracks on the Fe-W sample surface during the corrosion tests (see Fig. 27b) can accelerate the dissolution of the Fe-W matrix. A slight decrease in the value of the corrosion current ( $i_{\text{corr}}$ ) is observed for the composite coatings as compared to the Fe-W sample, see Table 2. Such behaviour could be related to a higher resistance to crack propagation as compared to the Fe-W sample, which is thought to be attributed to the presence of the alumina particles (see Fig. 27b and 27c). However, the Fe-W/Al<sub>2</sub>O<sub>3</sub> coatings have a lower corrosion resistance when compared to chrome coatings (several studies report a corrosion current for chrome coating, measured in marine environments, in the range of 10<sup>-6</sup> A/cm<sup>2</sup> [104,105] which is two order of magnitude lower than the corrosion current measured for Fe-W alloys, see Table 2). A suggestion on how to improve the corrosion resistance of Fe-W alloys is presented in chapter 7.

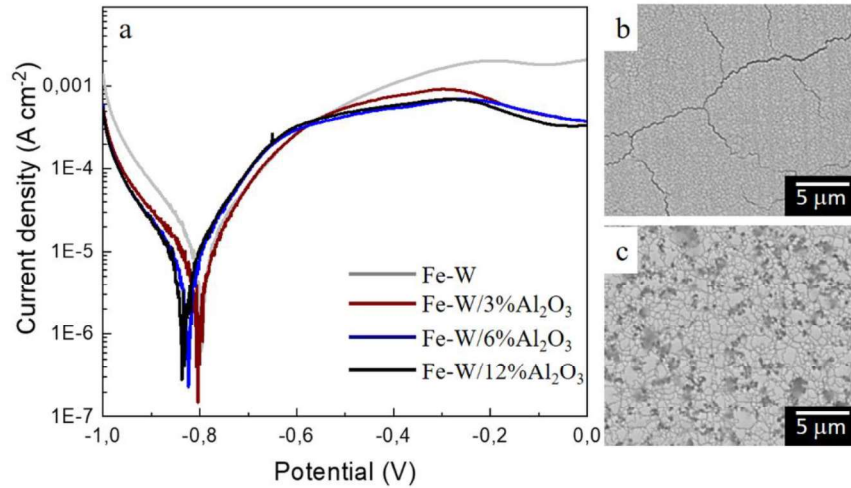


Figure 27. Linear sweep voltammograms (a) for Fe-W and Fe-W/Al<sub>2</sub>O<sub>3</sub> composite coatings and SEM images of Fe-W (b) and Fe-W/12%Al<sub>2</sub>O<sub>3</sub> coatings (c) after corrosion test in 0.1M NaCl at room temperature.

Table 2 Extracted corrosion parameters from the voltammograms shown in Figure 27.

Sample	-E <sub>corr</sub> (V)	-J <sub>corr</sub> (A/cm <sup>2</sup> )
Fe-W	0.8	5 x 10 <sup>-4</sup>
Fe-W/3%Al <sub>2</sub> O <sub>3</sub>	0.8	3 x 10 <sup>-4</sup>
Fe-W/6%Al <sub>2</sub> O <sub>3</sub>	0.82	3 x 10 <sup>-4</sup>
Fe-W/12%Al <sub>2</sub> O <sub>3</sub>	0.84	3 x 10 <sup>-4</sup>

In summary, the acquired results highlight the beneficial effect of the co-deposition of alumina particles in the Fe-W matrix for the wear resistance of the composite coatings. In particular, the composite containing 12% of Al<sub>2</sub>O<sub>3</sub> particles showed promising results, i.e. lowest COF and wear rate. Thus, this specimen was selected as the most competitive sustainable replacement of hard Cr coatings. In the following paragraph, the wear resistance of the composite coating and of electrodeposited hard Cr is compared, both in as-deposited condition and after annealing treatment at 600 °C. As described in Paper VI, the co-deposition of 12% Al<sub>2</sub>O<sub>3</sub> particles enhanced the wear resistance, but also resulted in a slight reduction of the mechanical properties of the composite as compared to the Fe-W coating. Hence, the heat treatment is performed for obtaining a coating with both optimized mechanical properties and wear resistance.

## 5.5 Mechanical and wear properties of annealed Fe-W/12%Al<sub>2</sub>O<sub>3</sub> composites

As described in chapter 5.1, annealing of the Fe-W/12%Al<sub>2</sub>O<sub>3</sub> composite at 600 °C led to the formation of  $\alpha$ -Fe crystalline phase and resulted in a mixed amorphous-nanocrystalline structure (see Fig. 2 in Paper VII). The  $\alpha$ -Fe crystallites formed after annealing can be seen in in Fig. 28b. In the SEM micrograph of the annealed coating (Fig. 28b), they appear as small white particles.

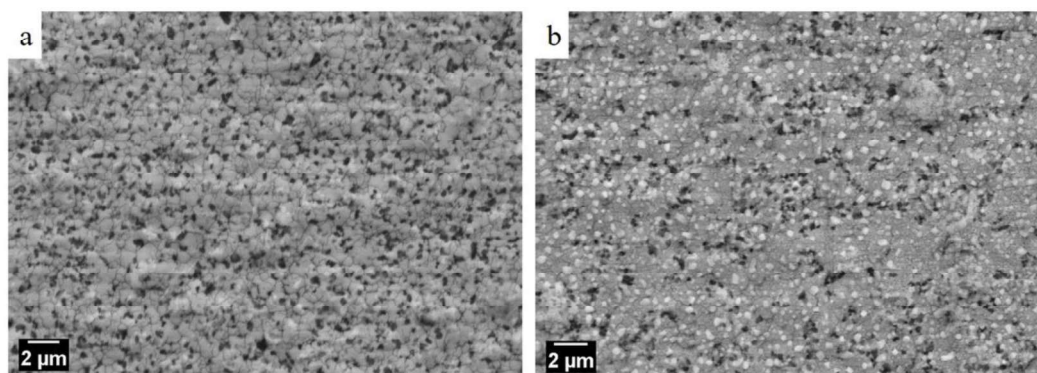


Figure 28. SEM micrographs of the surface of the Fe-W/12%Al<sub>2</sub>O<sub>3</sub> coatings in the as-deposited condition (a) and after annealing at 600 °C (b).

Electrodeposited Cr coatings were also annealed at 600 °C before measuring the mechanical properties and the wear resistance of the coatings. The variation of the hardness upon annealing is shown in Fig. 29, whereas the COF and the wear rate are shown in Fig. 30. The hardness of both Fe-W/12%Al<sub>2</sub>O<sub>3</sub> and hard Cr coatings is strongly affected by the annealing treatment, see Fig. 29. The hardness of the composite coatings significantly increases up to 16.3 GPa, whereas a 50% decrease is observed in the hardness of hard Cr coatings. For the composite coatings the hardness increase can be related to the partial crystallization of the Fe-W matrix, which results in the formation of a mixed amorphous-nanocrystalline structure as described in the paragraph 5.2. The decrease in the hardness of heat-treated Cr coatings can be related to grain growth, as observed in previous studies [106]. The heat treatment reduces also the wear resistance of hard Cr coatings. In fact, the wear rate increases from  $\sim 4 \times 10^{-6}$  up to  $\sim 24 \times 10^{-6}$  mm<sup>3</sup>/Nm, see Fig. 30. In turn, the wear resistance of the composite coatings is preserved upon annealing, i.e. the COF and wear rate for the as-deposited and annealed coatings are almost identical. The slight increase in the COF observed after annealing can be related to an increase in the surface roughness due to the formation of the  $\alpha$ -Fe grains.

In summary, the obtained results show that heat treatments of Fe-W/Al<sub>2</sub>O<sub>3</sub> composite coatings can be applied to further enhance the mechanical properties of the coating while preserving the wear resistance. In fact, in the applied experimental conditions the annealed Fe-W/12%Al<sub>2</sub>O<sub>3</sub> composite coatings are characterized with mechanical properties and wear resistance which are superior to the properties of as-deposited hard Cr coatings. The combination of good mechanical properties and high wear resistance obtained in the annealed Fe-W/Al<sub>2</sub>O<sub>3</sub> composite coatings represents an important step towards the development of competitive and sustainable alternatives for hard Cr coatings.

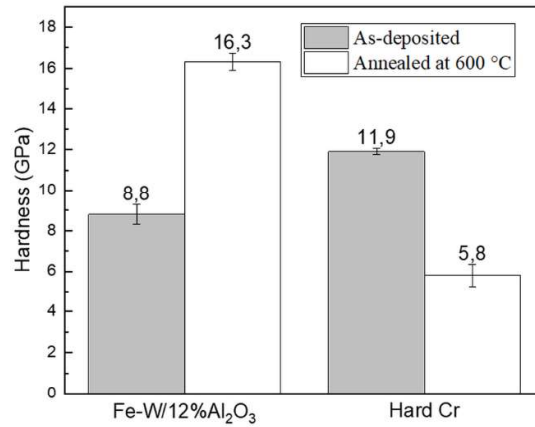


Figure 29. Hardness of Fe-W/12%Al<sub>2</sub>O<sub>3</sub> and hard Cr coatings in the as-deposited state and after annealing at 600 °C.

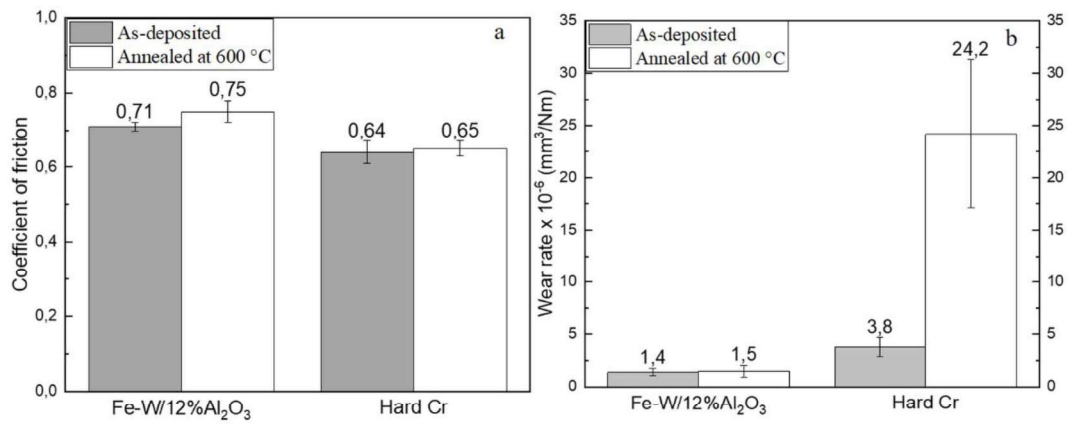


Figure 30 Coefficient of friction (a) and wear rate (b) of Fe-W/12%Al<sub>2</sub>O<sub>3</sub> and hard Cr coatings in the as-deposited state and after annealing at 600 °C.



## 6 Conclusions

This thesis focuses on the characterization of Fe-W alloys which are electrodeposited with a sustainable approach. In fact, a properly developed electrolytic bath is used for the deposition of the coatings: minimally invasive, thermodynamically stable, and without toxic compounds. The main goal of the thesis is to evaluate the interactions between the materials characteristic (e.g. composition and structure) and the properties of interest, i.e. mechanical properties, as well as wear and corrosion resistance. In connection to the research questions formulated in chapter 1.2, the following conclusions (summarized in Fig. 31 and 32) were obtained:

RQ1: How is the composition (i.e. the W content) influencing the structure and the thermal stability of Fe-W coatings?

RQ2: How are composition and structure influencing the hardness of Fe-W coatings?

- An increase of the W-content leads to a transition from a nanocrystalline structure, as observed for the Fe-4W coating, to a homogeneous amorphous structure, as observed for the Fe-24W coating.
- An increase of the W-content leads to enhanced thermal stability of the material. For the Fe-24W coating, a large fraction of the amorphous structure is preserved upon annealing at 600 °C for 1 hour and complete crystallization is not even reached after annealing at 800 °C for 12 hours.
- The co-deposited O present in the Fe-4W and Fe-16W samples causes the precipitation of FeWO<sub>4</sub> phase upon vacuum annealing at 800 °C. Annealing at 800 °C in a slightly oxidizing atmosphere (i.e. Ar atmosphere) favours the crystallization of the oxide also in the Fe-24W coating.
- The Fe-24W coating shows the highest hardness and reduced elastic modulus both in the as-deposited and annealed condition.
- For the Fe-24W coating, the maximum hardness and elastic modulus are obtained after annealing at 600 °C for 1 hour, due to the formation of  $\alpha$ -Fe crystallites in the Fe-W amorphous matrix.
- Annealing the Fe-24W and the Fe-16W coatings at 800 °C for 1 hour leads to a reduction in hardness due to the growth of the  $\alpha$ -Fe grains. For the Fe-4W sample, a reduction in the hardness is observed already at 600 °C.

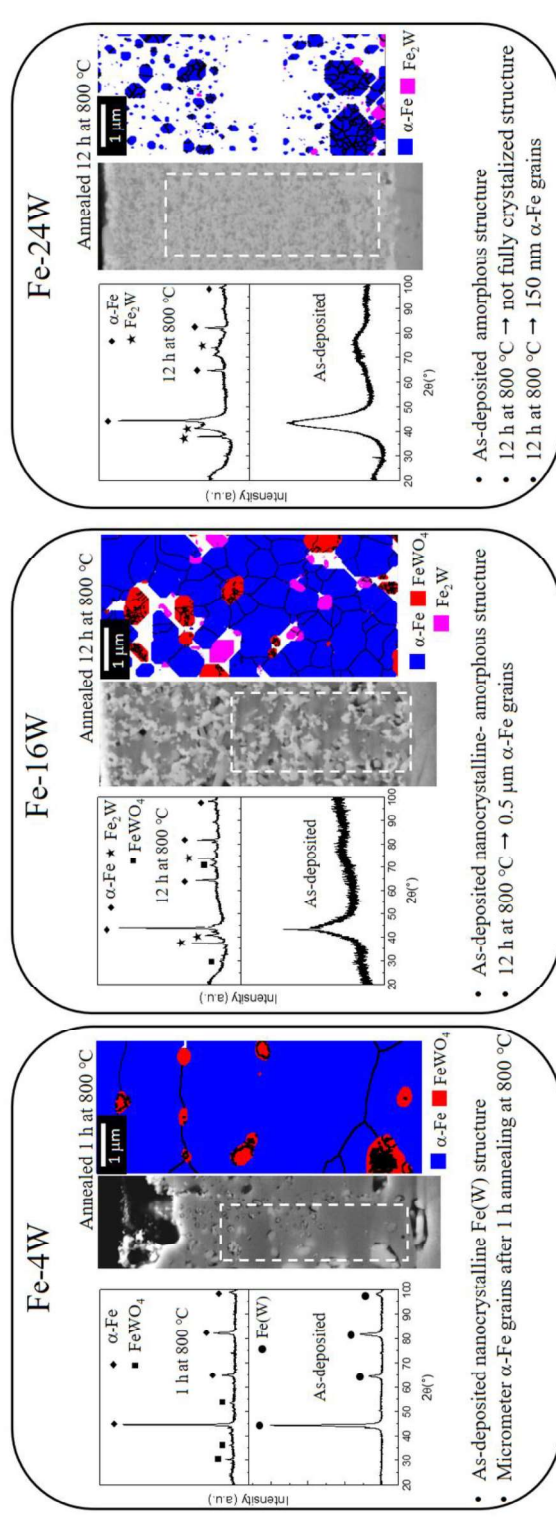
RQ3: What is the main factor determining the wear and corrosion resistance of Fe-W coatings? Can such properties be improved with the co-deposition of hard particles such as Al<sub>2</sub>O<sub>3</sub>?

RQ4: Which combination of material characteristics and annealing treatments results in optimum hardness and wear resistance in Fe-W alloys? Are such properties comparable to the hardness and wear resistance of hard Cr coatings?

- Tribo-oxidation is found to be the main factor influencing the wear of as-deposited and annealed Fe-24W coatings. The severe tribo-oxidation observed for the Fe-24W samples annealed between 200 and 600 °C caused the formation of deep cracks along the wear track (i.e.  $\sim$ 15  $\mu$ m in depth).
- The formation of the Fe<sub>2</sub>W and FeWO<sub>4</sub> phases upon annealing of Fe-24W samples at 800 °C increases the resistance to tribo-oxidation which results into a considerable reduction of the wear rate.

- The co-deposition of  $\text{Al}_2\text{O}_3$  particles favours the grain size refinement and the amorphization of the Fe-W matrix.
- The co-deposition of  $\text{Al}_2\text{O}_3$  particles enhances the wear resistance of the Fe-W matrix. In particular, the composite containing the highest amount of particle, i.e. 12vol.%  $\text{Al}_2\text{O}_3$ , is characterized with the lowest COF and wear rate.
- The influence of the co-deposited alumina particles on the corrosion resistance is limited. The corrosion occurs through Fe dissolution and the formation of Fe and W oxygen compounds.
- The co-deposited alumina particles do not influence the microstructural transformation of the Fe-W matrix upon annealing at 600 °C, where part of the Fe-W matrix crystallizes with the formation of  $\alpha$ -Fe.
- Annealing treatments result in a substantial increase in the hardness and the Young's modulus of the Fe-W/12% $\text{Al}_2\text{O}_3$ . Under the same conditions, the hardness of the Cr coating considerably decreases.
- The wear resistance of the composite coatings is preserved upon annealing, whereas a significant increase in the wear rate of hard Cr coatings is observed. In the applied experimental conditions, the mechanical properties and wear resistance of Fe-W/12% $\text{Al}_2\text{O}_3$  composite coatings, especially after annealing, are superior to the properties of as-deposited hard Cr coatings.

## Co-deposited W content



## Thermal stability

Figure 31 Summary of the main results in relation to the research question RQ1. In the schematic plot is shown the effect of W content on the structure and thermal stability of Fe-W coatings

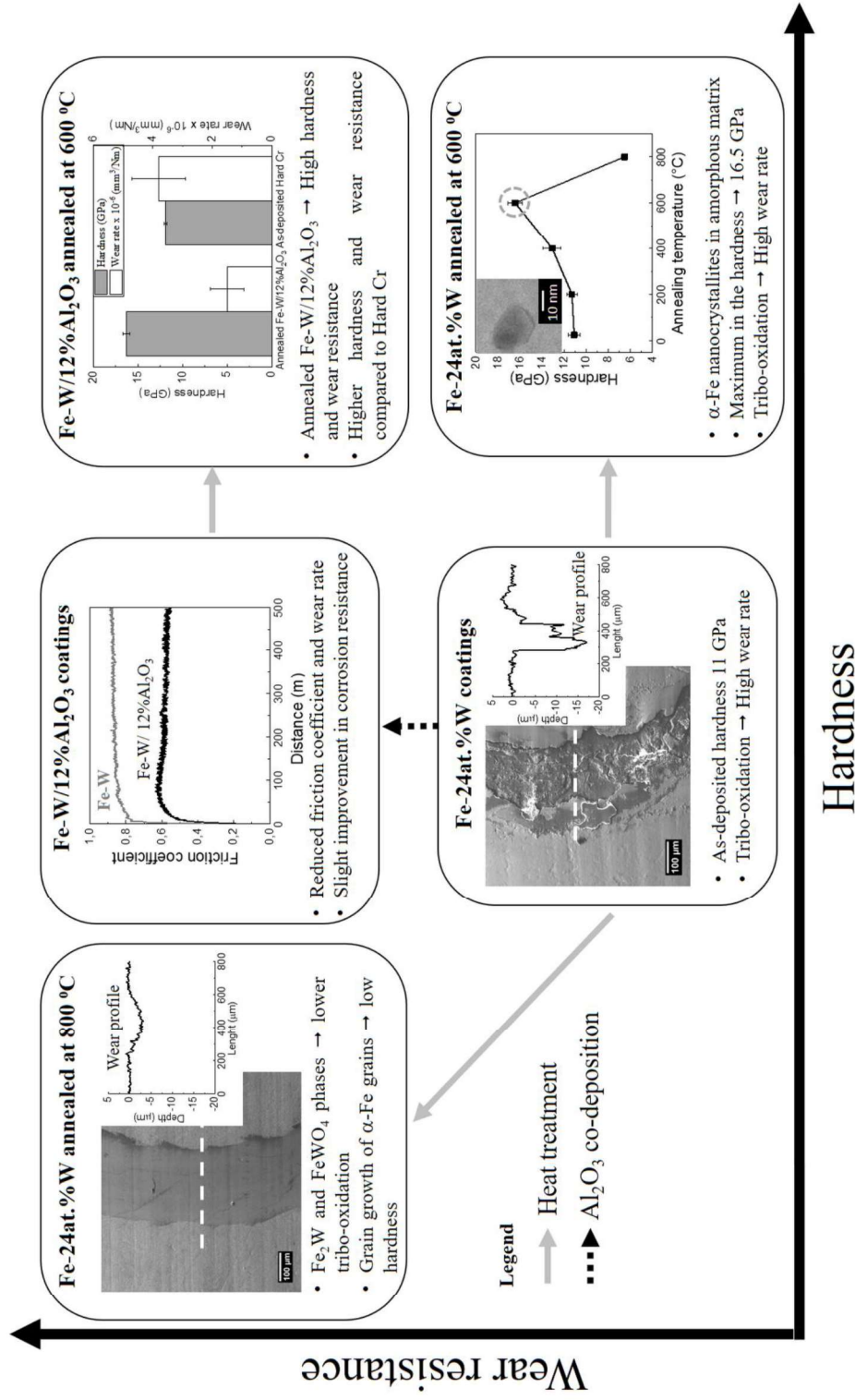


Figure 32 Summary of the main results in relation to the research question RQ2, RQ3, and RQ4. In the schematic plot is shown the effect of heat treatments and of the Al<sub>2</sub>O<sub>3</sub> co-deposition on the hardness and wear resistance of Fe-W alloys.

## 7 Future work

In consideration of the results presented in this thesis work, the following aspects are suggested for continuation of the work:

- The electrolytes used for the electrodeposition of the Fe-W alloys studied in this thesis did not contain organic additives. It would be interesting to study the effect of organic additives, e.g. grain-refiners, on the deposition of Fe-W alloys. With the addition of grain-refiners, it could be possible to deposit nanocrystalline and/or amorphous Fe-W coatings with lower W content. A decrease in the co-deposited W content would result in a lower environmental impact of the produced coatings.
- The deposition of Fe-W alloys was performed with the application of direct current. It would be interesting to study the effects of different electrodeposition techniques, i.e. pulse plating and/or reverse pulse plating. There are several advantages when performing pulse plating, e.g. better surface finishing of the deposit, more uniform deposit thickness and grain size refinement, among others. Improvements in the surface finishing would be beneficial for the up-scaling and marketing of Fe-W coatings. The beneficial effects of grain refinement have been already pointed out above.
- Promising results have been obtained with respect to mechanical properties and wear resistance of the studied Fe-W alloys. However, improvements are required regarding the corrosion resistance of the Fe-W alloys especially when compared to the corrosion resistance of chrome coatings. Studying the addition of Sn as a ternary alloying element to enhance the corrosion resistance of the Fe-W alloys would be of interest. Sn is often added as alloying element in corrosion resistant coatings, and its use would also meet sustainability concerns expressed in Paper I (i.e. Sn is not listed as CRM or as a SVHC and it can be recovered from metal scraps).
- The study of Fe-W alloys could also be extended towards magnetic properties. A paper from Nicolenco et al. [81] revealed that as-deposited coatings with relative low W content (i.e. between 5 and 14at.% of W) are characterized with a good combination of mechanical and magnetic properties which could be of interest for various microelectromechanical systems. The study could be extended including the analysis of how heat treatments affect the magnetic properties of such coatings. Relaxation and recrystallization mechanisms occurring upon annealing can result in an improvement of the magnetic properties [107].



## 8 Acknowledgements

First and foremost I would like to thank my supervisor and examiner Uta Klement for her guidance and support and for always pushing me to do better. You could always find time for a meeting or even for a short discussion, and for that I am deeply grateful.

For the financial support I acknowledge the European Union's Horizon 2020 research and innovation program under the Marie Skłodowska-Curie grant agreement (n° 665919) SELECTA project. My sincere gratitude goes to all the people involved in the SELECTA project. The friendship and network that we built over these years are of great importance to me.

I would like to especially thank several people I had the pleasure to work with:

- Aliona Nicolenco for her passion and commitment in studying Fe-W coatings. I could always count on you for planning and discussing experiments. For all the help I received, I thank you.
- Natalya Tsyntsaru and Henrikas Cesiulis for hosting me at Vilnius University and for all the valuable feedbacks and research advices.
- Jordi Sort, Eva Pellicer and Jordina Fornell from Autonomous University of Barcelona. Thank you for hosting me, for the kind collaboration and for your critical reviews and suggestions.
- Naroa Imaz and Vanesa Martinez-Nogues for helping me at CIDETEC with the wear measurements. Also, thank you Naroa for all the tips and suggestions during my stay at San Sebastian.
- Inga Ennen and Andreas Hütten for the work done together with the in situ TEM at Bielefeld University. Thank you for being so supportive and determined even against the bad luck.
- Eric Tam, Yiming Yao and Roger Sagdahl for their support and for all the (countless) time they helped me in the lab.

I want to thank all the colleagues at the Department of Industrial and Materials Science for creating such a nice working environment and for the enjoyable time together. A special thanks goes to my friends Casey Jessop, Camille Pauzon, Dmitri Riabov, Philipp Hoier and William Hearn for all the amazing time and good laughs we had together. I want to thank my friends of a lifetime, Alberto, Baldo, Eleonora, Enrico, Marta, Roberto, Toni e Ugo. No matter the distance, I can always count on our friendship.

Thank you Ena, for all the love and support I receive every day. Thank you for making Göteborg my new home (wherever our next home will be).

Finally, I want to thank my brother Alberto and my parents Angelo and Rosalba. Thank you for everything. I wouldn't be who I am today without your endless love.



## 9 References

1. Elkington, G.; Elkington, H. Improvements in Coating, Covering, or Plating certain Metals. 1840.
2. Erb, U.; El-Sherik, A.M.; Palumbo, G.; Aust, K.T. Synthesis, structure and properties of electroplated nanocrystalline materials. *Nanostructured Mater.* **1993**, *2*, 383–390.
3. Robertson, A.; Erb, U.; Palumbo, G. Practical applications for electrodeposited nanocrystalline materials. *Nanostructured Mater.* **1999**, *12*, 1035–1040.
4. <https://www.futuremarketinsights.com/reports/electroplating-market> (accessed on Aug 21, 2019).
5. Larson, C. Global comparisons of metal finishing sectors: Part 2, some technology and operational variations. *Trans. Inst. Met. Finish.* **2012**, *90*, 232–236.
6. Schlesinger, M.; Paunovic, M. *Modern Electroplating, 5th edition*; Schlesinger, M., Paunovic, M., Eds.; John Wiley & Sons, Inc., 2010; ISBN 9780470167786.
7. Tyler, J.M. Automotive applications for chromium. *Met. Finish.* **1995**, 11–14.
8. Giurlani, W.; Zangari, G.; Gambinossi, F.; Passaponti, M.; Salvietti, E.; Di Benedetto, F.; Caporali, S.; Innocenti, M. Electroplating for decorative applications: Recent trends in research and development. *Coatings* **2018**, *8*, 1–25.
9. Schwarzacher, W. Electrodeposition: A technology for the future. *Electrochem. Soc. Interface* **2006**, *15*, 32–33.
10. Zangari, G. Electrodeposition of Alloys and Compounds in the Era of Microelectronics and Energy Conversion Technology. *Coatings* **2015**, *5*, 195–218.
11. Zangari, G. Electrodeposition for energy conversion: Electrochemistry over matter. *Electrochem. Soc. Interface* **2011**, *20*, 31–32.
12. Pierre, F.; Diebold, F.; Baruthio, F. Biomonitoring of two types of chromium exposure in an electroplating shop. *Int. Arch. Occup. Environ. Heal.* **2008**, *81*, 321–329.
13. Baral, A.; Engelken, R.; Stephens, W.; Farris, J.; Hannigan, R. Evaluation of aquatic toxicities of chromium and chromium-containing effluents in reference to chromium electroplating industries. *Arch. Environ. Contam. Toxicol.* **2006**, *50*, 496–502.
14. Vasudevan, S.; Oturan, M.A. Electrochemistry: As cause and cure in water pollution-an overview. *Environ. Chem. Lett.* **2014**, *12*, 97–108.
15. Council directive 2002/95/EC on the restriction of the use of certain hazardous substances in electrical and electronic equipment. *Off. J. Eur. Union* **2003**, L37/19.
16. <http://www.un.org/sustainabledevelopment/> (accessed on Feb 15, 2018).
17. <https://www.un.org/sustainabledevelopment/news/communications-material/> (accessed on Feb 21, 2020).
18. Regulation concerning the Registration, Evaluation, Authorization and Restriction of Chemicals (REACH). *Off. J. Eur. Union* **2006**, L 136/3.
19. <https://echa.europa.eu/candidate-list-table> (accessed on Feb 21, 2020).
20. <https://echa.europa.eu/authorisation-list> (accessed on Oct 28, 2019).

21. Beral, A.; Engelken, R. Modeling, optimization, and comparative analysis of trivalent chromium electrodeposition from aqueous glycine and formic acid baths. *J. Electrochem. Soc.* **2005**, *157*.
22. Ghosh, S.K.; Celis, J.P. Tribological and tribocorrosion behaviour of electrodeposited CoW alloys and CoW-WC nanocomposites. *Tribol. Int.* **2013**, *68*, 11–16.
23. Chen, L.; Wang, L.; Zeng, Z.; Xu, T. Influence of pulse frequency on the microstructure and wear resistance of electrodeposited Ni-Al<sub>2</sub>O<sub>3</sub> composite coatings. *Surf. Coatings Technol.* **2006**, *201*, 599–605.
24. Eskin, S.; Berkh, O.; Rogalsky, G.; Zahavi, J. Co-W Alloys for Replacement of Conventional Hard Chromium. *Plat. Surf. Finish.* **1998**, *85*, 79–83.
25. Wasekar, N.P.; Sundararajan, G. Sliding wear behavior of electrodeposited Ni – W alloy and hard chrome coatings. *Wear* **2015**, *342–343*, 340–348.
26. de Lima-Neto, P.; da Silva, G.P.; Correia, A.N. A comparative study of the physicochemical and electrochemical properties of Cr and Ni-W-P amorphous electrocoatings. *Electrochim. Acta* **2006**, *51*, 4928–4933.
27. Weston, D.P.; Harris, S.J.; Capel, H.; Ahmed, N.; Shipway, P.H.; Yellup, J.M. Nanostructured Co-W coatings produced by electrodeposition to replace hard Cr on aerospace components. *Trans. Inst. Met. Finish.* **2010**, *88*, 47–56.
28. Denkhaus, E.; Salnikow, K. Nickel essentiality, toxicity, and carcinogenicity. *Crit. Rev. Oncol. Hematol.* **2002**, *42*, 35–56.
29. Seilkop, S.K.; Oller, A.R. Respiratory cancer risks associated with low-level nickel exposure: An integrated assessment based on animal, epidemiological, and mechanistic data. *Regul. Toxicol. Pharmacol.* **2003**, *37*.
30. [http://europa.eu/rapid/press-release\\_IP-13-658\\_en.htm](http://europa.eu/rapid/press-release_IP-13-658_en.htm) (accessed on Feb 15, 2018).
31. Grilli, M.L.; Bellezze, T.; Gamsjäger, E.; Rinaldi, A.; Novak, P.; Balos, S.; Piticescu, R.R.; Ruello, M.L. Solutions for critical raw materials under extreme conditions: A review. *Materials (Basel)*. **2017**, *10*, 1–23.
32. Tkaczyk, A.H.; Bartl, A.; Amato, A.; Lapkovskis, V.; Petranikova, M. Sustainability evaluation of essential critical raw materials: Cobalt, niobium, tungsten and rare earth elements. *J. Phys. D. Appl. Phys.* **2018**, *51*.
33. Communication from the Commission to the European Parliament, the Council, the European Economic and Social Committee and the Committee of the Regions: on the 2017 list of Critical Raw Materials for the EU. *Off. J. Eur. Union* **2017**, *8*.
34. Gamburg, Y.D.; Zangari, G. *Theory and Practice of Metal Electrodeposition*; 2011; ISBN 9788578110796.
35. Fischer, H. Wirkungen der Inhibitoren bei der Elektrokristallisation. *Electrochim. Acta* **1960**, *2*, 50–96.
36. Zajkoska, S.P.; Mulone, A.; Hansal, W.E.G.; Klement, U.; Mann, R.; Kautek, W. Alkoxylated  $\beta$ -Naphthol as an Additive for Tin Plating from Chloride and Methane Sulfonic Acid Electrolytes. *Coatings* **2018**, *8*, 79.
37. Brenner, A.; Burkhead, P.; Seegmiller, E. Electrodeposition of Tungsten Alloys

- Containing Iron, Nickel, and Cobalt. *J. Res. Natl. Bur. Stand. (1934)*. **1947**, *39*, 351–384.
38. Fischer, H. Electrocrystallization of Metals under Ideal and Real Conditions. *Angew. Chemie Int. Ed. English* **1969**, *8*, 108–119.
  39. Zhang, Y. Tin and Tin Alloys for Lead-Free Solder. *Mod. Electroplat. Fifth Ed.* **2011**, 139–204.
  40. Fischer, H. *Elektrolytische Abscheidung und Elektrokristallisation von Metallen*; Springer: Berlin, 1954;
  41. Winand, R. Electrocrystallization - theory and applications. *Hydrometallurgy* **1992**, *29*, 567–598.
  42. Erb, U.; Aust, K.T.; Palumbo, G. Electrodeposited Nanocrystalline Metals, Alloys, and Composites. *Nanostructured Mater. Second Ed.* **2007**, 235–292.
  43. Palumbo, G.; Thorpe, S.J.; and Aust, K.T. On the contribution of triple junctions to the structure and properties of nanocrystalline materials. *Scr. Metall. Mater.* **1990**, *24*, 1347–1350.
  44. McMahan, G.; Erb, U. Structural transitions in electroplated Ni-P alloys. *J. Mater. Sci. Lett.* **1989**, *8*, 865–868.
  45. Trelewicz, J.R.; Schuh, C.A. The Hall-Petch breakdown in nanocrystalline metals: A crossover to glass-like deformation. *Acta Mater.* **2007**, *55*, 5948–5958.
  46. Schuh, C.A.; Nieh, T.G.; Yamasaki, T. Hall-Petch breakdown manifested in abrasive wear resistance of nanocrystalline nickel. *Scr. Mater.* **2002**, *46*, 735–740.
  47. Schuh, C.A.; Nieh, T.G.; Iwasaki, H. The effect of solid solution W additions on the mechanical properties of nanocrystalline Ni. *Acta Mater.* **2003**, *51*, 431–443.
  48. Jafary-Zadeh, M.; Kumar, G.P.; Branicio, P.S.; Seifi, M.; Lewandowski, J.J.; Cui, F. A critical review on metallic glasses as structural materials for cardiovascular stent applications. *J. Funct. Biomater.* **2018**, *9*, 1–32.
  49. Kruzic, J.J. Bulk Metallic Glasses as Structural Materials: A Review. *Adv. Eng. Mater.* **2016**, *18*, 1308–1331.
  50. Scully, R.; Gebert, A.; Payer, J.H. Corrosion and related mechanical properties of bulk metallic glasses. *J. Mater. Res.* **2007**, *22*, 302–313.
  51. Golt'z, L.N.; Kharlamov, V.. N.. Electrolytic deposition of alloys of tungsten, nickel and copper from water solutions. *Zhur. Priklad. Khim.* **1936**, *9*, 640–652.
  52. Holt, M.L. The codeposition of tungsten and iron from aqueous solutions. *Trans. Electrochem. Soc.* **1934**, *66*, 453–458.
  53. Eliaz, N.; Eliezer, G. Induced Codeposition of Alloys of Tungsten, Molybdenum and Rhenium with Transition Metals. *Mod. Asp. Electrochem.* **2008**, 191–301.
  54. Weston, D.P.; Harris, S.J.; Shipway, P.H.; Weston, N.J.; Yap, G.N. Establishing relationships between bath chemistry, electrodeposition and microstructure of Co-W alloy coatings produced from a gluconate bath. *Electrochim. Acta* **2010**, *55*, 5695–5708.
  55. Tsyntsar, N.; Cesiulis, H.; Donten, M.; Sort, J.; Pellicer, E.; Podlaha-Murphy, E.J. Modern trends in tungsten alloys electrodeposition with iron group metals. *Surf. Eng.*

- Appl. Electrochem.* **2013**, *48*, 491–520.
56. Nishi, Y.; Mogi, Y.; Oguri, K.; Watanabe, T. Preparation of Fe-W amorphous films by an electroplating method. *J. Mater. Sci. Lett.* **1995**, *20*, 1–3.
  57. Donten, M.X.; Cesiulis, H.; Stojek, Z. Electrodeposition and properties of Ni-W, Fe-W and Fe-Ni-W amorphous alloys. A comparative study. *Electrochim. Acta* **2000**, *45*, 3389–3396.
  58. Chou, M.C.; Chu, C.F.; Wu, S.T. Phase transformations of electroplated amorphous iron-tungsten-carbon film. *Mater. Chem. Phys.* **2003**, *78*, 59–66.
  59. Rupert, T.J.; Schuh, C.A. Sliding wear of nanocrystalline Ni-W: Structural evolution and the apparent breakdown of Archard scaling. *Acta Mater.* **2010**, *58*, 4137–4148.
  60. Chianpairot, A.; Lothongkum, G.; Schuh, C.A.; Boonyongmaneerat, Y. Corrosion of nanocrystalline Ni-W alloys in alkaline and acidic 3.5wt.% NaCl solutions. *Corros. Sci.* **2011**, *53*, 1066–1071.
  61. Rupert, T.J.; Trelewicz, J.R.; Schuh, C.A. Grain boundary relaxation strengthening of nanocrystalline Ni-W alloys. *J. Mater. Res.* **2012**, *27*, 1285–1294.
  62. Vamsi, M.V.N.; Wasekar, N.P.; Sundararajan, G. Influence of heat treatment on microstructure and mechanical properties of pulse electrodeposited Ni-W alloy coatings. *Surf. Coatings Technol.* **2017**, *319*, 403–414.
  63. Vamsi, M.V.N.; Wasekar, N.P.; Sundararajan, G. Sliding wear of as-deposited and heat-treated nanocrystalline nickel-tungsten alloy coatings. *Wear* **2018**, *412–413*, 136–143.
  64. Jinlong, L.; Zhuqing, W.; Tongxiang, L.; Suzuki, K.; Hideo, M. Effect of tungsten on microstructures of annealed electrodeposited Ni-W alloy and its corrosion resistance. *Surf. Coatings Technol.* **2018**, *337*, 516–524.
  65. Sunwang, N.; Wangyao, P.; Boonyongmaneerat, Y. The effects of heat treatments on hardness and wear resistance in Ni-W alloy coatings. *Surf. Coatings Technol.* **2011**, *206*, 1096–1101.
  66. Tsyntaru, N.; Cesiulis, H.; Pellicer, E.; Celis, J.P.; Sort, J. Structural, magnetic, and mechanical properties of electrodeposited cobalt-tungsten alloys: Intrinsic and extrinsic interdependencies. *Electrochim. Acta* **2013**, *104*, 94–103.
  67. Weston, D.P.; Shipway, P.H.; Harris, S.J.; Cheng, M.K. Friction and sliding wear behaviour of electrodeposited cobalt and cobalt-tungsten alloy coatings for replacement of electrodeposited chromium. *Wear* **2009**, *267*, 934–943.
  68. Capel, H.; Shipway, P.H.; Harris, S.J. Sliding wear behaviour of electrodeposited cobalt – tungsten and cobalt – tungsten – iron alloys. **2003**, *255*, 917–923.
  69. Vernickaite, E.; Tsyntaru, N.; Cesiulis, H. Electrodeposition and corrosion behaviour of nanostructured cobalt-tungsten alloys coatings. *Trans. Inst. Met. Finish.* **2016**, *94*, 313–321.
  70. Ghaferi, Z.; Raeissi, K.; Golozar, M.A.; Edris, H. Characterization of nanocrystalline Co-W coatings on Cu substrate, electrodeposited from a citrate-ammonia bath. *Surf. Coatings Technol.* **2011**, *206*, 497–505.
  71. Su, F.; Liu, C.; Huang, P. Friction and wear of nanocrystalline Co and Co-W alloy

- coatings produced by pulse reverse electrodeposition. *Wear* **2013**, *300*, 114–125.
72. Tsyntsaru, N.I.; Bobanova, Z.I.; Kroitoru, D.M.; Cheban, V.F.; Poshtaru, G.I.; Dikusar, A.I. Effect of a multilayer structure and lubrication on the tribological properties of coatings of Fe-W alloys. *Surf. Eng. Appl. Electrochem.* **2010**, *46*, 538–546.
  73. Tsyntsaru, N.; Bobanova, J.; Ye, X.; Cesiulis, H.; Dikusar, A.; Prosycevas, I.; Celis, J.P. Iron-tungsten alloys electrodeposited under direct current from citrate-ammonia plating baths. *Surf. Coat. Technol.* **2009**, *203*, 3136–3141.
  74. Bobanova, Z.I.; Dikusar, A.I.; Cesiulis, H.; Celis, J.-P.; Tsyntsaru, N.I.; Prosycevas, I. Micromechanical and Tribological Properties of Nanocrystalline Coatings of Iron-Tungsten Alloys Electrodeposited from Citrate-Ammonia Solutions. *Russ. J. Electrochem.* **2009**, *45*, 895–901.
  75. Wang, S.; Zeng, C.; Ling, Y.; Wang, J.; Xu, G. Phase transformations and electrochemical characterizations of electrodeposited amorphous Fe–W coatings. *Surf. Coatings Technol.* **2016**, *286*, 36–41.
  76. Barbano, E.P.; Carlos, I.A.; Vallés, E. Electrochemical synthesis of Fe-W and Fe-W-P magnetic amorphous films and Fe-W nanowires. *Surf. Coatings Technol.* **2017**, *324*, 80–84.
  77. Gamburg, Y.; Zakharov, E.; Goryunov, G. Electrodeposition, structure, and properties of iron–tungsten alloys. *Russ. J. Electrochem* **2001**, *37*, 670–673.
  78. Donten, M. Bulk and surface composition, amorphous structure, and thermocrystallization of electrodeposited alloys of tungsten with iron, nickel, and cobalt. *J. Solid State Electrochem.* **1999**, *3*, 87–96.
  79. Donten, M.; Cesiulis, H.; Stojek, Z. Electrodeposition of amorphous/nanocrystalline and polycrystalline Ni-Mo alloys from pyrophosphate baths. *Electrochim. Acta* **2005**, *50*, 1405–1412.
  80. Lietzke, M.H.; and Holt, M.L. Codeposition of tungsten and iron from aqueous ammoniacal citrate bath. *J. Electrochem. Soc.* **1948**, *94*, 252.
  81. Nicolenco, A.; Tsyntsaru, N.; Fornell, J.; Pellicer, E.; Reklaitis, J.; Baltrunas, D.; Cesiulis, H.; Sort, J. Mapping of magnetic and mechanical properties of Fe-W alloys electrodeposited from Fe(III)-based glycolate-citrate bath. *Mater. Des.* **2018**, *139*, 429–438.
  82. Yar-Mukhamedova, G.; Ved, M.; Sakhnenko, N.; Karakurkchi, A.; Yermolenko, I. Iron binary and ternary coatings with molybdenum and tungsten. *Appl. Surf. Sci.* **2016**, *383*, 346–352.
  83. Tsyntsaru, N.; Dikusar, A.; Cesiulis, H.; Celis, J.P.; Bobanova, Z.; Sidel’Nikova, S.; Belevskii, S.; Yapontseva, Y.; Bersirova, O.; Kublanovskii, V. Tribological and corrosive characteristics of electrochemical coatings based on cobalt and iron superalloys. *Powder Metall. Met. Ceram.* **2009**, *48*, 419–428.
  84. Nicolenco, A.; Tsyntsaru, N.; Cesiulis, H. Fe (III)-Based Ammonia-Free Bath for Electrodeposition of Fe-W Alloys. *J. Electrochem. Soc.* **2017**, *164*, D590–D596.
  85. Goldstein, J.I.; Newbury, D.E.; Echlin, P.; Joy, D.C.; Lyman, C.E.; Lifshin, E.; Sawyer, L.; Michael, J.R. *Scanning Electron Microscopy and X-ray Microanalysis*; Third

- Edition, Ed.; Springer, 2005; ISBN 9781461349693.
86. Schwartz, A.J.; Kumar, M.; Adams, B.L.; Field, D.P. *Electron Backscatter Diffraction in Materials Science*; Springer, 2009; ISBN 9780387881355.
  87. Maitland, T.; Sitzman, S. Electron Backscatter Diffraction (EBSD) Technique and Materials Characterization Examples. *Scanning Microsc. Nanotechnol. Tech. Appl.* **2007**, 41–76.
  88. Hornbogen, E. *Durchstrahlungs-Elektronenmikroskopie fester Stoffe*; Verlag Chemie GmbH, 1971;
  89. da Silva, M. Thermal Stability of Electrodeposited Nanocrystalline Ni- and Co-Based Materials, Chalmers University of Technology, 2007.
  90. Oliver, W.C.; Pharr, G.M. Measurement of hardness and elastic modulus by instrumented indentation: Advances in understanding and refinements to methodology. *J. Mater. Res.* **2004**, 19, 3–20.
  91. Ma, E.; Zhang, Z. Amorphous alloys: Reflections from the glass maze. *Nat. Mater.* **2011**, 10, 10–11.
  92. He, F.; Yang, J.; Lei, T.; Gu, C. Structure and properties of electrodeposited Fe-Ni-W alloys with different levels of tungsten content: A comparative study. *Appl. Surf. Sci.* **2007**, 253, 7591–7598.
  93. Jacob, A.; Schmetterer, C.; Singheiser, L.; Gray-Weale, A.; Hallstedt, B.; Watson, A. Modeling of Fe-W phase diagram using first principles and phonons calculations. *Calphad Comput. Coupling Phase Diagrams Thermochem.* **2015**, 50, 92–104.
  94. Antoni-Zdziobek, A.; Commeau, T.; Joubert, J.M. Partial redetermination of the Fe-W phase diagram. *Metall. Mater. Trans. A Phys. Metall. Mater. Sci.* **2013**, 44, 2996–3003.
  95. Hou, K.; Chang, Y.; Chang, S.; Chang, C. The heat treatment effect on the structure and mechanical properties of electrodeposited nano grain size Ni – W alloy coatings. *Thin Solid Films* **2010**, 518, 7535–7540.
  96. Mun, S.-J.; Kim, M.; Yim, T.-H.; Lee, J.-H.; Kang, T. Mechanical and Structural Characteristics of Electrodeposited Ni-Fe-W Alloy after Heat-Treatment. *J. Electrochem. Soc.* **2010**, 157, D177–D180.
  97. Fornell, J.; González, S.; Rossinyol, E.; Suriñach, S.; Baró, M.D.; Louzguine-Luzgin, D. V.; Perepezko, J.H.; Sort, J.; Inoue, A. Enhanced mechanical properties due to structural changes induced by devitrification in Fe-Co-B-Si-Nb bulk metallic glass. *Acta Mater.* **2010**, 58, 6256–6266.
  98. Wang, J.G.; Choi, B.W.; Nieh, T.G.; Liu, C.T. Crystallization and nanoindentation behavior of a bulk Zr-Al-Ti-Cu-Ni amorphous alloy. *J. Mater. Res.* **2000**, 15, 798–807.
  99. Schuh, C.A.; Hufnagel, T.C.; Ramamurty, U. Mechanical behavior of amorphous alloys. *Acta Mater.* **2007**, 55, 4067–4109.
  100. Chong, X.Y.; Jiang, Y.H.; Zhou, R.; Zhu, H.; Feng, J. Electronic structure, anisotropic elastic and thermal properties of the  $\eta$  phase F6W6C. *Comput. Mater. Sci.* **2015**, 108, 205–211.
  101. Abdel-Aal, H.A. On the interdependence between kinetics of friction-released thermal

- energy and the transition in wear mechanisms during sliding of metallic pairs. *Wear* **2003**, *254*, 884–900.
102. Yılmaz, G.; Hapçı, G.; Orhan, G. Properties of Ni/Nano-TiO<sub>2</sub> Composite Coatings Prepared by Direct and Pulse Current Electroplating. *J. Mater. Eng. Perform.* **2014**, *24*, 709–720.
  103. He, J.; He, F.L.; Li, D.W.; Liu, Y.L.; Yin, D.C. A novel porous Fe/Fe-W alloy scaffold with a double-layer structured skeleton: Preparation, in vitro degradability and biocompatibility. *Colloids Surfaces B Biointerfaces* **2016**, *142*, 325–333.
  104. Imaz, N.; Ostra, M.; Vidal, M.; Díez, J.A.; Sarret, M.; García-Lecina, E. Corrosion behaviour of chromium coatings obtained by direct and reverse pulse plating electrodeposition in NaCl aqueous solution. *Corros. Sci.* **2014**, *78*, 251–259.
  105. Li, X.L.; Liu, X.H.; Tian, H. Bin; Yuan, W.J. Experimental research on hard and crack-free electrodeposited chromium coatings. *Adv. Mater. Res.* **2014**, *1044–1045*, 47–52.
  106. Brittain, C.P.; Smith, G.C. The Influence of Annealing on the Structure and Hardness of Electrodeposited Chromium. *Trans. IMF* **1954**, *31*, 146–152.
  107. Yi, Y.; Peng, Y.; Xia, C.; Wu, L.; X., K.; Nie, J. Influence of heat treatment on microstructures and magnetic properties of Fe-based soft magnetic composites prepared by co-precipitation method. *J. Magn. Magn. Mater.* **2019**, *476*, 100–105.